IOP Publishing | International Atomic Energy Agency Nuclear Fusion

Nucl. Fusion 55 (2015) 104017 (20pp) doi:10.1088/0029-5515/55/10/104017

DIII-D research to address key challenges for ITER and fusion energy

R.J. Buttery[1] and the DIII-D Team

[1] General Atomics, PO Box 85608, San Diego, CA 92186–5608, USA

E-mail: buttery@fusion.gat.com

Received 24 January 2015, revised 1 May 2015
Accepted for publication 6 May 2015
Published 29 July 2015

Abstract

DIII-D has made significant advances in the scientific basis for fusion energy. The physics mechanism of resonant magnetic perturbation (RMP) edge localized mode (ELM) suppression is revealed as field penetration at the pedestal top, and reduced coil set operation was demonstrated. Disruption runaway electrons were effectively quenched by shattered pellets; runaway dissipation is explained by pitch angle scattering. Modest thermal quench radiation asymmetries are well described NIMROD modelling. With good pedestal regulation and error field correction, low torque ITER baselines have been demonstrated and shown to be compatible with an ITER test blanket module simulator. However performance and long wavelength turbulence degrade as low rotation and electron heating are approached. The alternative QH mode scenario is shown to be compatible with high Greenwald density fraction, with an edge harmonic oscillation demonstrating good impurity flushing. Discharge optimization guided by the EPED model has discovered a new super H-mode with doubled pedestal height. Lithium injection also led to wider, higher pedestals. On the path to steady state, 1 MA has been sustained fully noninductively with $\beta_N = 4$ and RMP ELM suppression, while a peaked current profile scenario provides attractive options for ITER and a $\beta_N = 5$ future reactor. Energetic particle transport is found to exhibit a critical gradient behaviour. Scenarios are shown to be compatible with radiative and snowflake divertor techniques. Physics studies reveal that the transition to H mode is locked in by a rise in ion diamagnetic flows. Intrinsic rotation in the plasma edge is demonstrated to arise from kinetic losses. New 3D magnetic sensors validate linear ideal MHD, but identify issues in nonlinear simulations. Detachment, characterized in 2D with sub-eV resolution, reveals a radiation shortfall in simulations. Future facility development targets burning plasma physics with torque free electron heating, the path to steady state with increased off axis currents, and a new divertor solution for fusion reactors.

Keywords: fusion, plasma, tokamak, energy

(Some figures may appear in colour only in the online journal)

1. Introduction

As magnetic confinement fusion moves to the reactor scale, key challenges exist to anticipate changes in plasma behaviour and develop robust scenario and control solutions. DIII-D confronts this challenge through its operational flexibility coupled with leading edge diagnostics and simulation, in order to resolve underlying physics and develop more effective techniques for fusion plasmas that project to reactor conditions. For ITER, key progress has been made in developing and understanding mitigation solutions for disruptions, edge localized modes (ELMs) and plasma instabilities, as well as predicting the changes in underlying physics and operating regimes at low torque and collisionality, and with electron heating. A major focus on scientific understanding is building confidence in underlying physics models to project to future devices, with key developments on turbulence, L–H transition, rotation, 3D field interactions and energetic particle physics. On the broader path to fusion energy, a range of fully noninductive scenarios provide promising candidates for ITER, a future nuclear science facility and a power plant, with key physics trade-offs identified. Innovative new approaches have been pioneered, such as the discovery of the super H-mode with doubled pedestal height. Research is also elucidating the physics of an improved detached divertor solution and associated materials, with innovative 2D imaging and material test techniques. Insights gained are helping to resolve underlying physical mechanisms, build confidence in projection and inform the development of better solutions in the advancement of fusion energy.

This paper is organized on a topical basis, starting with the most urgent issues for ITER. Section 2 concentrates on the achievement and physics behind ELM control and improved pedestal. Section 3 addresses disruption mitigation. In section 4 we explore how core behaviour changes under increasingly burning plasma-like conditions, while section 5 deals with the development of robust scenarios for ITER and underlying stability issues. We then turn towards issues of fusion energy, with development of high performance steady state core plasmas in section 6, and the physics basis for improved boundary solutions in section 7. Section 8 concludes with an overview of achievements and discussion of the future direction for the DIII-D programme.

1.1. Facility capabilities and improvements

The DIII-D programme is founded on a high level of operational flexibility, so that it can understand the physics and more closely match conditions of future devices. This includes high shaping and 3D field capabilities (18 poloidal field (PF) coils and 18 '3D' perturbative field coils), asymmetric upper and lower divertors, as well as independent power, torque, electron : ion heating, density, and deposition control through heating and current drive systems with co/counter and on/off axis neutral beam injectors, steerable electron cyclotron heating and current drive systems, and three cryopumps. These are accompanied by a comprehensive state of the art diagnostics suite to identify physics mechanisms behind observed behaviours.

Results in 2013–14 have further capitalized on several enhancements of the facility. New disruption mitigators and associated diagnostics were used in developing the physics understanding and resolving control tool choices in support of ITER proposed techniques. Electron cyclotron deposition control, using steerable mirrors, real time fitting and deposition calculations, has enabled automated tracking and suppression of modes in several scenarios, notably aiding high β fully noninductive operation and low torque ITER baseline plasmas. A major 3D magnetics upgrade has identified key physics and models governing both global plasma response to perturbative 3D-field, and local mechanisms by which such fields suppress ELMs. In addition, the main ion charge exchange recombination (CER) is now providing crucial constraints to transport, pedestal and rotation models. A new lithium dropper has led to improvements in pedestal performance. Finally, a periscope with infra-red and visible systems, together with newly developed coherence imaging of flows and centre post swing probes have been used in combination with high resolution sub-eV 2D-mapping divertor Thomson scattering to identify the physics of detachment, revealing a radiative shortfall in detachment models.

2. Achieving a robustly ELM-stable and high performance pedestal

The tokamak pedestal is the critical area governing plasma performance, establishing the basis for core fusion performance, but giving rise to ELMs, which must be mitigated to avoid first wall erosion. DIII-D has expanded access to ELM-suppressed regimes, developed new higher performance pedestals and answered critical physics questions.

2.1. Suppression of ELMs by RMPs

By exploiting DIII-D's flexible 3D field coil arrays and upgraded magnetics, it has for the first time been possible to identify experimentally that penetration of resonant fields at the pedestal top is the physical mechanism by which

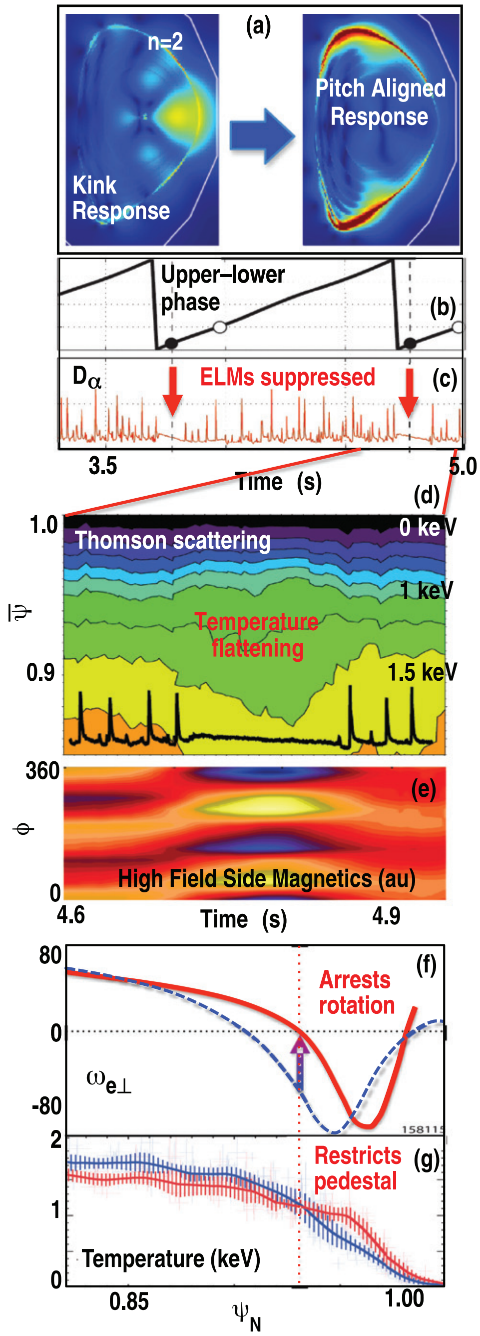

Figure 1. Response to RMP and field penetration leading to ELM suppression: (a) varying $n = 2$ field from pressure drive kink to pitch-aligned kink response (IPEC simulation), (b) $n = 2$ upper-lower RMP phase rotation, (c) ELM suppression observed in D_α light, (d) Thomson scattering observes temperature flattening at pedestal top, (e) high-field side magnetics observe bifurcation in pitch-resonant field, (f) perpendicular electron rotation tends to zero at the pedestal top on ELM suppression, (g) pedestal becomes narrower.

RMPs suppress ELMs [1, 2] (figure 1). This was achieved by extending the technique to $n = 2$ RMPs, which allowed the field structure to be continuously varied by rotating the phase differential between $n = 2$ fields from an upper coil array and a lower coil array (figure 1(b)). This led to periods of ELM suppression and ELMing activity (figure 1(c)).

The ELM suppression phase coincides with ideal MHD modelling indicating a pitch-aligned plasma response to the field, localized near the edge of the plasma (figure 1(a), right image, from the IPEC code). Conversely modelling between the ELM suppression phases (figure 1(a), left image, taken for fields applied midway between suppression phases) shows a global kink like response that is dominant on the outboard side and mid radii in the plasma. This indicates that the plasma responds differently to different types field, with multiple modes capable of being excited, and suggests that the RMP-ELM suppression mechanism is associated with pitch resonant field interactions near the plasma edge (consistent with driving a tearing interaction at the pedestal top). Crucially, the transition to ELM suppression is accompanied by a nonlinear increase in magnetic response in new high-field side magnetic measurements (figure 1(e)), consistent with a field line pitch-resonant field developing associated with a transition from shielding to island formation. This leads to a decrease in temperature and pressure gradients near the pedestal top, as observed on high resolution Thomson scattering measurements (figure 1(d)) limiting pedestal width, consistent with island formation at the pedestal top. With pedestal pressure gradient limited by kinetic ballooning modes (KBM), the resulting restriction on pedestal height (shown also in the electron temperature profile in figure 1(g) maintains the pedestal below the non-local kink-ballooning stability limit at which ELMs are triggered [3].

This interpretation, of penetration of RMP to induce islands at the pedestal top, is confirmed by measurements of perpendicular electron rotation (figure 1(f)), with magnitude strongly reduced at the pedestal top, consistent with stationary island formation at this location (as is also seen with $n = 3$ RMP ELM suppression). It is also strongly supported by two fluid MHD calculations with the M3D-C1 code, which predict a significant enhancement of the tearing drive at the top of the pedestal in the ELM-suppressed phase. Here, stochastization due to island formation at multiple closely spaced rational surfaces is predicted to increase cross-field transport in this region [4]. This leads to a predominantly $n = 0$ predicted profile response, also explaining the lack of a clear observed helical island structure when suppression occurs. Encouragingly, these simulations predict the same effect in ITER [5, 6].

Further confidence in the technique is gained from the successful application of $n = 3$ RMP ELM suppression as successive coils are turned off (figure 2) [7], while maintaining suppression at similar coil current and confinement levels. M3D-C1 simulation indicates that the reduction in the primary $n = 3$ harmonic is compensated by additional $n = 2$, 4 and 5 sidebands. Type I ELM control with RMPs has also been extended to low torque helium plasmas with dominant electron heating, as shown in figure 3, providing an important validation for the ITER research plan, which seeks to establish the basis for ELM suppression in its non-nuclear phase. The ELM type in these high-purity helium plasmas is confirmed by their rising frequency with heating power in matched plasmas without RMPs, consistent with the scaling of type I ELMs in deuterium plasmas. Finally, in the fully noninductive regime of the steady state hybrid (described in section 6.2) RMPs are found to lead to a factor 5 reduction in ELM size, offering promise for future steady-state devices.

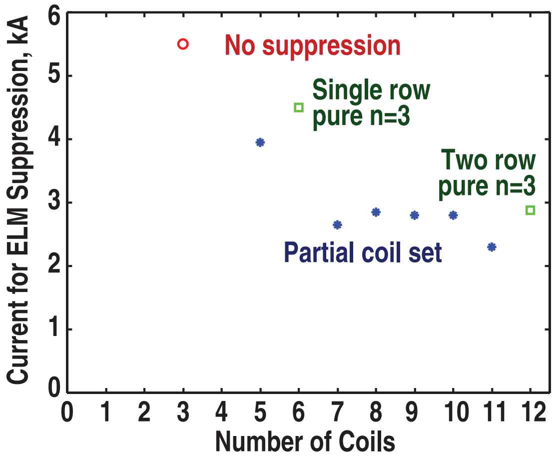

Figure 2. Current required for ELM suppression as decreasing number of coils used for RMP-ELM suppression in deuterium plasmas.

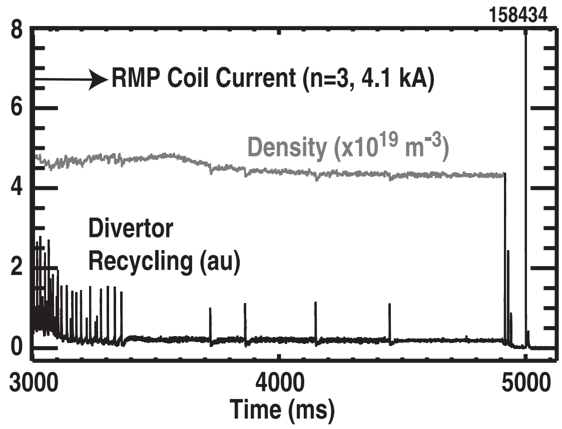

Figure 3. Suppression of type I ELMs in helium plasmas with an RMP field switched on at 3000 ms: D_α emission and line average density after RMP turned on at 3000 ms.

Across the database for RMP-ELM suppression, behaviour is consistent with the EPED model [3, 8, 9] of a peeling–ballooning limit governing ELM onset, with data and model showing pedestal pressure increasing with density and good confinement in cases that are close to RMP threshold for ELM suppression. The effects on confinement are described in figure 4, which shows that suppression can be achieved close to the EPED predicted maximum pedestal height (figure 4(a)) leading to good to confinement (figure 4(b)). However it is also possible to overdrive the RMP leading to confinement degradation, evident in the open symbols located below the trend. Encouragingly, impurities are not observed to accumulate in RMP ELM-suppressed plasmas, as discussed in the next subsection in comparison to other regimes.

2.2. Expanding performance of non-ELMing regimes

Significant advances have also been made in developing the QH mode regime for ELM-stable high performance operation [10, 11]. This regime is sustained by an edge harmonic oscillation (EHO) which replaces the ELM, sitting close to the peeling–ballooning limit (more specifically,

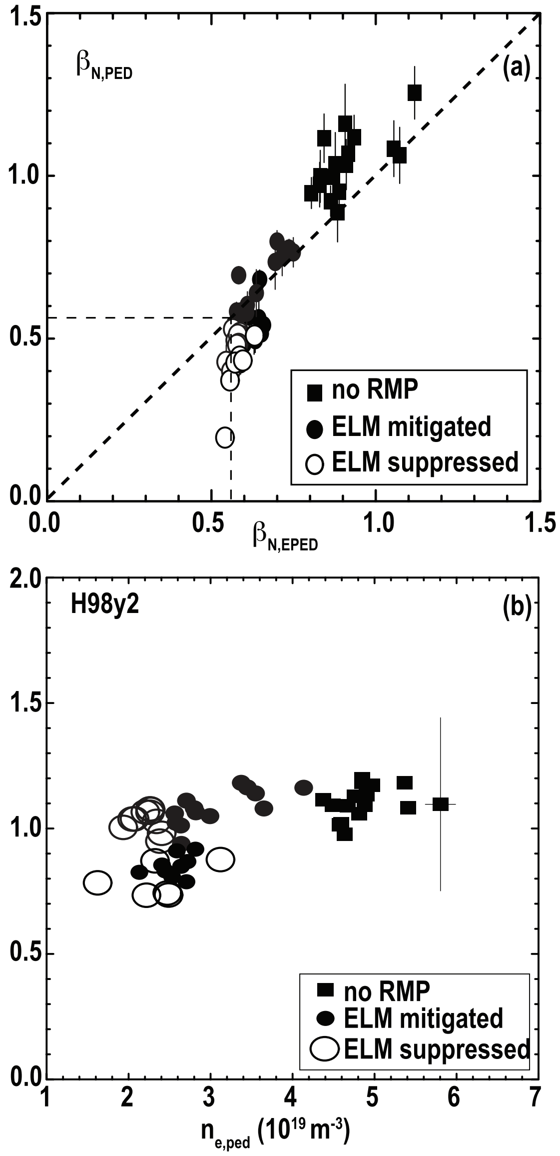

Figure 4. (a) Comparison of pedestal height in terms of pedestal β_N with EPED prediction as RMPs increased to achieve ELM mitigation and then suppression, and (b) effect on H factor versus pedestal density.

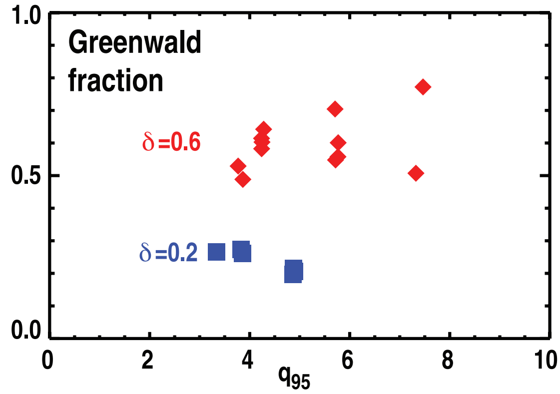

Figure 5. Extension of QH mode to high Greenwald density by changing plasma triangularity δ.

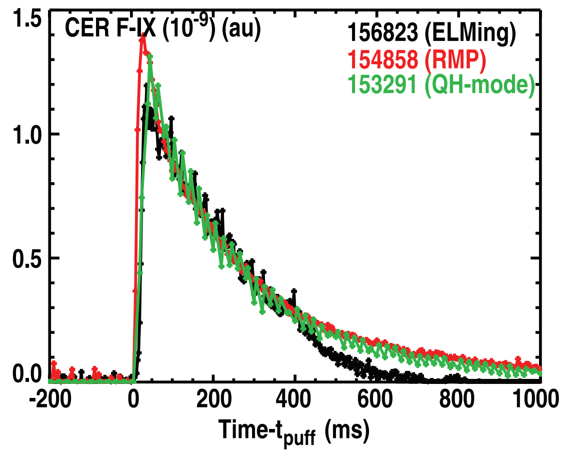

Figure 6. CER fluorine emission decay measurements after a small fluorine gas puff, indicating impurity flushing in ELMing (40 Hz for $t < 400$ ms), QH-mode and RMP ELM-suppressed H-mode.

the current-driven kink-peeling part of this limit). By increasing plasma shaping and fuelling, it has been possible to extend QH mode to high Greenwald density fraction (figure 5), establishing compatibility of the EHO with high density regimes. This validates the EPED description of QH mode access [3], which further projects that the ITER pedestal density will be in the correct range to access this regime. Nonlinear JOREK modelling of DIII-D QH-mode plasmas [12] predict the occurrence of saturated peeling–ballooning modes in the vicinity of the pedestal top, suggesting these account for the observed EHO. This modelling predicts that the EHO saturation mechanism is based on formation of magnetic islands and an ergodic layer at the pedestal top, although this has yet to be determined experimentally. This hypothesis contrasts with previous theories of saturation based on loss of rotation shear, which had been thought to be important in driving the EHO, and appeared to be a requirement experimentally [9]; further experiments are needed to resolve this question.

In addition to regulating edge electron transport, the EHO, based on CER measurements of fluorine confinement time, is found to give adequate levels of impurity flushing, comparable to 40 Hz ELMs in DIII-D and RMP ELM-suppression. figure 6 shows the comparison of the fluorine exhaust by these three mechanisms displaying their equivalence, with each achieving fluorine confinement times around 320 ms, as measured by the decay of fluorine levels after a puff of fluorine gas. This is much shorter than the case of low frequency (10–15 Hz) unmitigated ELMs in the ITER baseline that possess impurity confinement longer than one second and are subject to impurity accumulation [13]. Further, QH-mode plasmas exhibit increased energy confinement as the neutral beam torque and rotation are reduced (where 3D fields are applied to increase edge rotation shear through neoclassical toroidal viscosity effects to maintain the QH mode regime). Importantly here, particle confinement time, τ_p (defined as core particle confinement inside the separatrix, and does not include any recycling effects), is found to be insensitive to the rotation, such that the ratio τ_p/τ_E actually decreases in the more reactor relevant range of low rotation [10].

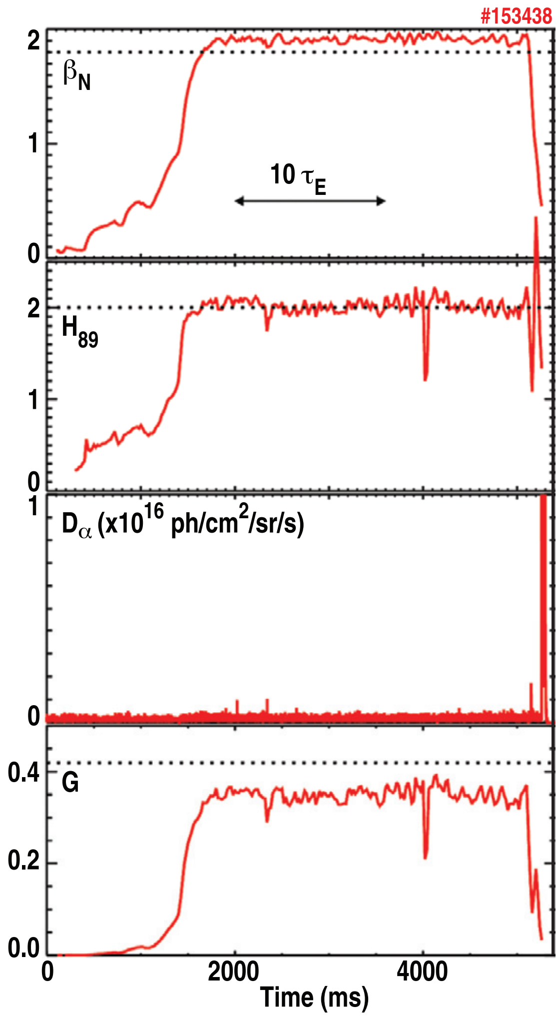

Figure 7. QH mode sustained operation at ITER target parameters for β_N and H_{89} (dashed line) and gain factor, $G = \beta_N H_{89}/q_{95}^2$ in counter rotation cases.

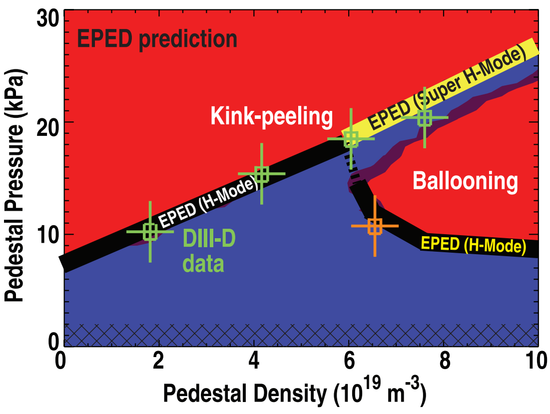

Figure 8. EPED predicted pedestal stability, in terms of pressure and density at the top of the pedestal, for plasmas with triangularity of 0.5 (blue = stable, red = unstable). Data points corresponding to access to super-H mode in DIII-D are added (green points) and to regular H mode (red point).

Performance of QH modes on DIII-D has also been demonstrated at the ITER baseline parameters, β_N, $H_{98pby,2}$ and q_{95} for 20 confinement times with strong counter rotation (figure 7). Work remains to extend the regime to suitable performance $\left(Q_{eq} \sim \beta_N H/q_{95}^2\right)$ at lower rotation with an ITER-relevant torque, where the key challenge is to achieve the required degree of stability at the necessary q_{95}. However, with confinement of QH-mode generally found to improve at lower rotation, it is anticipated that the performance goal can be met once the path to stable operation is resolved.

Further optimization of the pedestal has led to a new regime of high performance, dubbed 'super-H mode' [14, 15] which doubles pedestal height at a given density over the usual H-mode pedestal. EPED predicts that, with strong shaping, the pedestal solution splits above a critical density, into standard H-mode (black region in figure 8) and higher performance Super H-mode (yellow region) regimes, due to improved pedestal stability between peeling-kink and ballooning branches of stability, amplified by the effects of the KBM constraint on the pressure gradient. A path to Super H-mode has been navigated as shown by the data points in figure 8, taking advantage of the benign EHO in a QH edge to smoothly increase the density until the Super H regime is reached, leading to $H_{98pby,2} \sim 1.4$ and β_N up to 3.1, a record for operation with a quiescent edge, though further core optimization is considered possible that may raise this more. Pedestal heights are double those on the ballooning branch (that correspond to standard H-mode), suggesting this an exciting approach for transforming prospects for fusion energy.

In a separate development, injection of lithium pellets also led to dramatic improvements in pedestal performance (figure 9), in this case by causing edge turbulence in the 50–100 kHz band to rise leading to a broader but much higher pedestal pressure and ELM-free periods up to 0.35 s [16]. The improved pedestal also allowed higher global confinement ($H_{98pby,2}$ up to 2.1) and reduced influx of intrinsic impurities, i.e. carbon and nickel.

2.3. H-mode pedestal physics, rotation and access

The EPED model [3, 10] provides an important tool in predicting pedestal height, both for pedestal optimization and ELM onset and suppression, as discussed above. While it has been validated on multiple devices, new experiments on DIII-D provide direct evidence for the mechanisms involved. The model proposes that the KBM places a limit on the pressure gradient, while pedestal width grows until a peeling–ballooning mode is encountered (triggering the ELM or EHO). Measurements of inter-ELM activity show a superposition of broadband density fluctuations and quasi-coherent fluctuations (QCFs), hypothesized to be a manifestation of KBM activity (figure 10(a)) [17]. The amplitude of the QCFs begins to rise when a given temperature gradient is reached, and subsequently track the pedestal temperature gradient evolution as shown in figure 10(b), consistent with predicted KBM behaviour and thresholds. Using beam emission spectroscopy (BES), the broadband density fluctuations including the QCF are found to be localized in the vicinity of the pedestal top (figure 10(c)), similar to previous observations [18]. It should be noted that given the uncertainties in EFIT separatrix location, and the finite beam lifetime and viewing volume spot size effects, the radial localization of the peak in fluctuations to either the pedestal top or the steep gradient remains

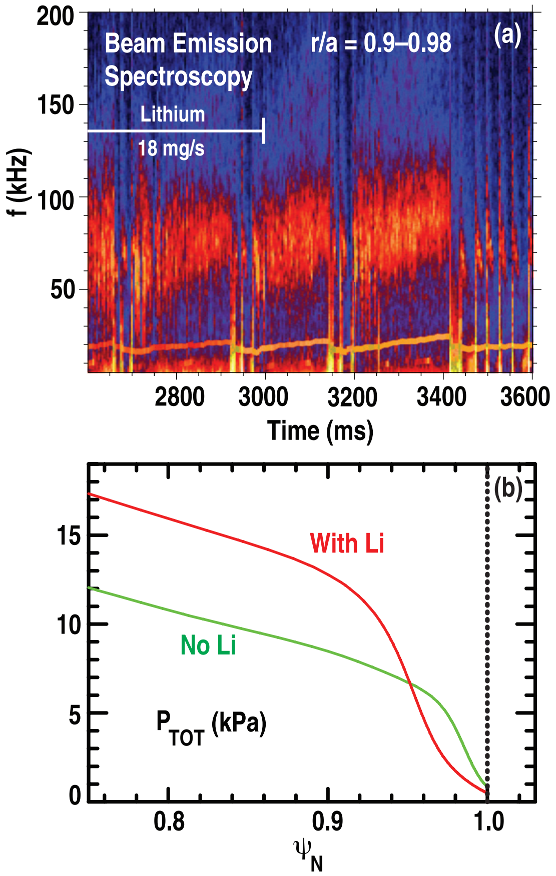

Figure 9. Injection of lithium by aerosol (time range and rate marked in (a)) leads to periods of increased turbulence between ELMs, evident here in the 50–100 kHz range with BES measurements of density fluctuations (a), associated with a broader and higher pedestal from fitted Thomson scattering pressure profiles (b).

unclear [17]. Similar correlations of the QCF with pedestal temperature gradient have also been observed on Alcator C-Mod [19]. This supporting evidence for the KBM role in pedestal physics gives further confidence in EPED as an effective tool for projecting to ITER.

Understanding the details of profiles, rotation generation, impurity transport and fuelling requires sophisticated, highly coupled physics. Here main ion CER and high resolution reciprocating probe measurements in electron cyclotron heated (ECH) H-mode (figure 11(a)) are consistent with a kinetic loss cone model of rotation generation, whereby asymmetric thermal ion losses from the distorted Maxwellian inside the plasma lead to an intrinsic rotation. New edge main ion CER measurements are consistent with and confirm the probe data, noting they are integrated over larger areas (figure 11(b)). Main ion measurements are critical in determining bulk rotation across the plasma, as they show dramatically different rotation levels from those inferred from carbon lines. Transport studies show this edge rotation correlates with rotation in the core, though effects of MHD and turbulence deeper inside can give rise to profile variations. A fuller description of the pedestal with XGC0 kinetic simulation provides greater insight [20, 21], showing energy and particle transport to be decoupled, with ion energy transport set primarily by collisionless orbit loss of deuterium ions in the thermal tail (validating the above concepts) while particle behaviour is governed by anomalous transport of colder bulk ions. It is expected that the kinetic effects that lead to intrinsic velocity near the separatrix in low collisionality plasmas on DIII-D will generate similar local edge flow velocities in ITER, though mapping to flux surface flows and the core remains a topic of further research.

Finally, turbulence diagnostics are providing critical understanding on the formation of the pedestal—the L–H transition. 2D BES measurements show how increased turbulence in an L-mode edge leads to increased Reynolds stress. This drives a sheared flow, which quenches the turbulence leading to the H-mode bifurcation when energy transfer to the driven flow exceeds the turbulence growth rate (figure 12) [22]. In some plasmas this leads to a cyclic behaviour (figure 13), where the H-mode only becomes sustained over longer timescales. Here Doppler backscattering (DBS) and CER capture the same turbulence-flow-generation effect, but the high flow shear state is not sustained, and the plasma periodically back-transitions. It is only after strong pedestal pressure gradients are established that the H mode becomes sustained, indicating the key role of pressure driven ion diamagnetic flow in locking in the H-mode transition through a rise in pressure-gradient-driven $E \times B$ shear [23]. Theoretical explanations invoke a predator–prey relationship of turbulence-driven meso-scale flows and turbulence [23, 24]. However, other theories suggest these transitions may be explainable purely through the mean field momentum transport equation [25, 26].

3. Disruption mitigation

Disruptions remain a key challenge for the tokamak, and one of the few remaining critical design issues for ITER, although design choices for ITER's auxiliary systems for disruption mitigation must be finalized in the next 2–3 years. Here, DIII-D research is establishing the principles and techniques for ITER's disruption mitigation system, not least with DIII-D being the only facility equipped with both ITER design options (massive gas injection (MGI) and shattered pellet injection (SPI)), and unique in studies of the more promising of the two techniques, SPI.

3.1. Runaway electron dissipation

A critical issue is the management of runaway electron (RE) beams, predicted to be strongly driven in ITER, requiring mitigation solutions to prevent ITER wall damage. New measurements indicate that the anomalously high rates of RE current dissipation observed during impurity injection into RE beams [27–29] are likely due to RE-ion pitch angle scattering, which is not accounted for in standard avalanche theory [27]. This understanding provides the physics basis for much more accurate modelling of RE dissipation scenarios in ITER. The improved measurements are enabled by a better methodology for reconstructing the RE plateau energy and pitch angle distribution functions using multiple diagnostics to span RE energies from keV to 10's MeV [30]. This method of measurement shows the favourability of high-Z (argon) MGI over mid-Z (neon) MGI in RE dissipation, as shown

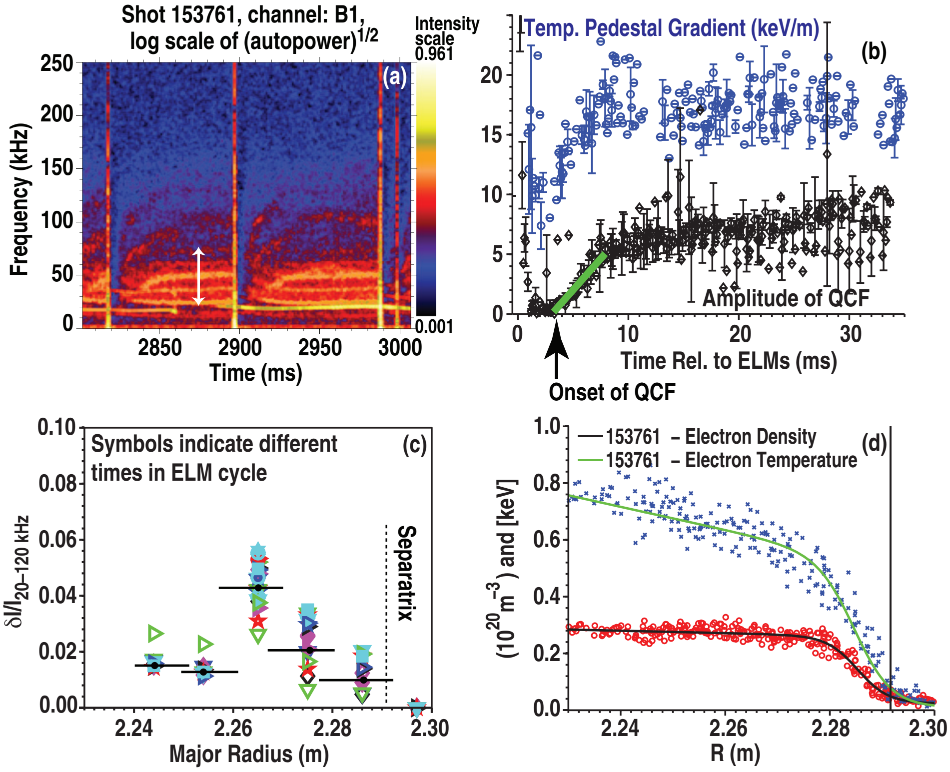

Figure 10. Fluctuation amplitude correlation with pedestal gradient evolution: (a) Magnetic fluctuation spectrogram; vertical arrow indicates the QCF frequency band to be considered for the amplitude analysis. (b) The QCF amplitude's evolution relative to ELM for the frequency bands 23–60 kHz. Overlaid in this plot is the temperature gradient evolution; the onset of the QCF amplitude evolution is indicated by the black arrow. (c) KBM-consistent density fluctuations in the pedestal region. (d) Thomson scattering profiles showing the pedestal top location.

in figure 14: while both species give significant reductions in the magnetic energy associated with the runaway beam, argon provides significantly stronger RE kinetic energy dissipation than mid-Z (neon) MGI [30]. The RE kinetic energy is observed to increase after neon injection due to the loop voltage induced by the resulting current dissipation, whereas argon completely dissipates the RE kinetic energy despite a large induced loop voltage. These results are highly encouraging that runaway dissipation can be obtained much more readily than previous more pessimistic predictions, though model development and validation is needed to provide confident projection for ITER.

Further, in a first-of-a-kind demonstration, RE seed suppression was attempted using a new ITER-prototype 'bent-tube' neon SPI system [31] fired into the early current quench. This process is designed to provide very high local impurity density for RE avalanche suppression using only moderate impurity input by firing solid neon fragments through the cold current quench (CQ) plasma so that they only ablate upon the small plasma volume occupied by the RE seed. Initial results show indications of RE seed suppression, with clear evidence from visible imaging that the SPI does penetrate the cold CQ plasma and ablate on the small core of seed REs. This process shows early promise as a viable method for RE suppression in ITER.

3.2. Thermal quench mitigation

Recent thermal quench (TQ) mitigation studies also provide encouragement for ITER [31, 32], with MGI not producing excessively localized heat loads from radiation asymmetry, validating NIMROD simulations [33, 34]. Studies with $n = 1$ error fields have confirmed the predicted importance of $n = 1$ mode activity during the pre-thermal quench (PTQ) and TQ in determining the radiation peaking following MGI [32, 34]. The measured peak toroidal peaking factor (TPF) when shifting the applied $n = 1$ field shot-to-shot (1.4 ± 0.2) agrees closely with the NIMROD predictions for DIII-D and ITER of $\sim$1.4 (figure 15). This level of toroidal asymmetry is not expected to be problematic for ITER. The initial phase of the mode immediately after MGI is found to originate 180° away from injector location [32, 35], consistent with NIMROD predictions [31].

Initial comparison of disruption mitigation using neon MGI to mitigation using the ITER prototype bent-tube neon SPI reveals several advantages of SPI over MGI. The SPI provides significantly greater radial penetration of the neon through the plasma boundary towards the plasma core prior to the thermal quench. This results in a larger fraction of the neon particles being retained within the plasma (higher particle assimilation) and increased impurity density. As a consequence, the neon SPI radiates a greater fraction of the initial plasma thermal energy than an equivalent quantity of neon MGI [32].

Finally, in the case of vertical displacement, mitigation of heat loads, forces and halo currents depended only modestly on injector poloidal location relative to displacement path, though earlier mitigation gave clear advantages in reducing heat loads from vertical displacement events (VDEs) [32].

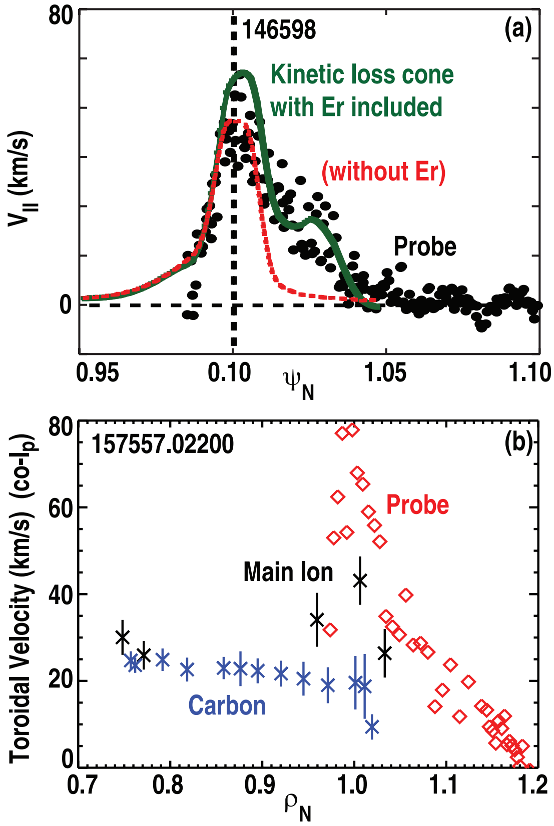

Figure 11. (a) Reciprocating probe measurements of parallel velocity confirm a kinetic intrinsic model rotation, (b) main ion CER shows significantly different velocities from carbon.

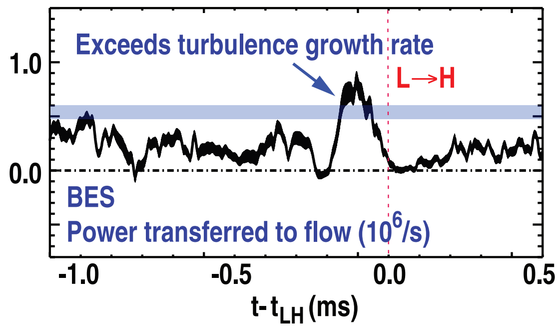

Figure 12. Transfer of power from turbulence to flow (as defined in reference [20] and measured by beam emission spectroscopy) exceeds a critical turbulence growth rate just before the L–H transition.

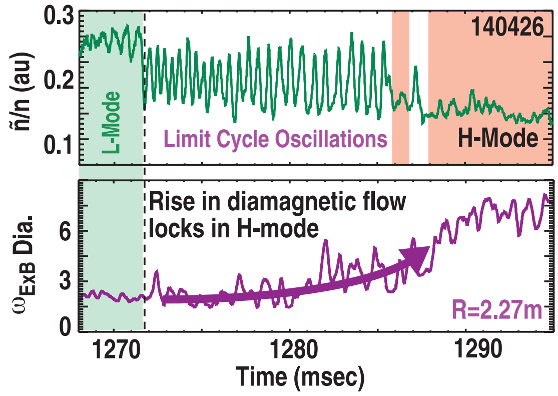

Figure 13. L–H limit cycle behaviour observed in BES density fluctuations (upper panel), and $E \times B$ rotation measurements (lower panel) indicating longer time-scale gradient rise.

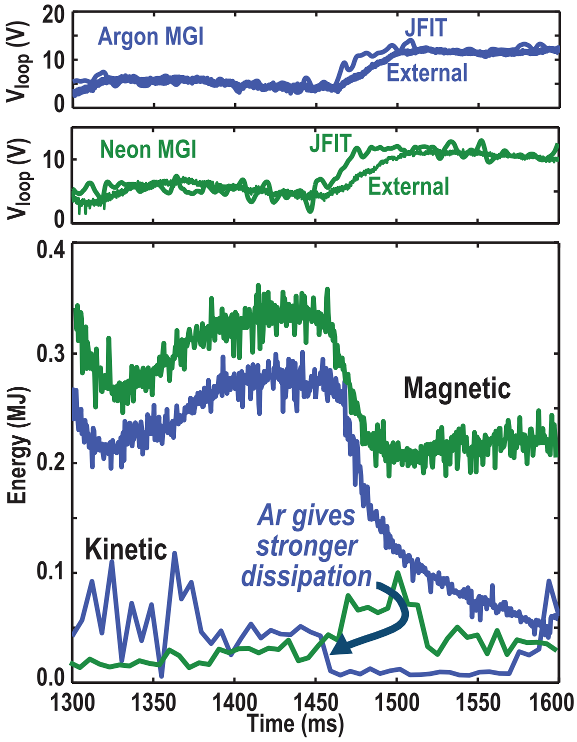

Figure 14. Loop voltages and stored energies for two shots with different species MGI quench mitigation. Argon MGI (blue) leads to greater dissipation of RE kinetic energy, than neon MGI (green) despite larger induced loop voltage.

4. Preparing for burning plasma conditions

Energy, particle and momentum transport will likely differ in burning plasmas compared with most present devices. Instead of high torque ion heating with core fuelling, burning plasmas will be heated through the electrons, without core fuelling or significant torque injection. This may lead to substantial changes in transport and stability, which must be understood if we are to re-optimize regimes for burning plasma conditions. DIII-D is confronting this challenge with neutral beam injection (NBI) torque control and ECH to access the relevant regimes, probe the physics and develop integrated scenario solutions, so that high performance burning plasmas can be readily achieved in ITER with confident projection capabilities.

4.1. Turbulent transport

A significant reduction in confinement is found in low torque ITER baseline-like plasmas when electron heating is applied, with $H_{98pby,2}$ falling from 1.02 to 0.88 when 3.3 MW of ECH is applied to a plasma with 3 MW neutral beam heating. Increasing T_e/T_i via ECH leads to increased particle loss and lower rotation, associated with large rises in low and intermediate k turbulence, with resulting profiles well matched by trapped gyro-Landau fluid (TGLF) calculation. To explore

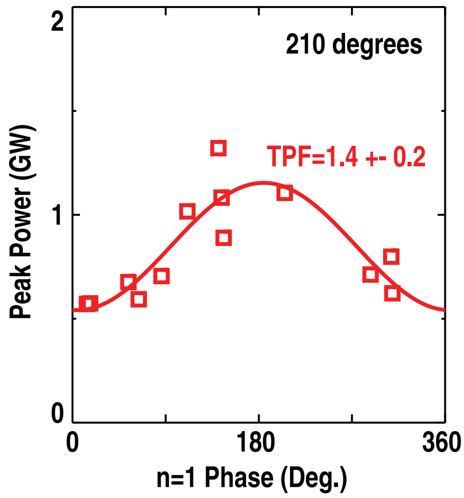

Figure 15. Measured radiated energy asymmetry during the disruption thermal quench, plotted against applied $n = 1$ error field phase.

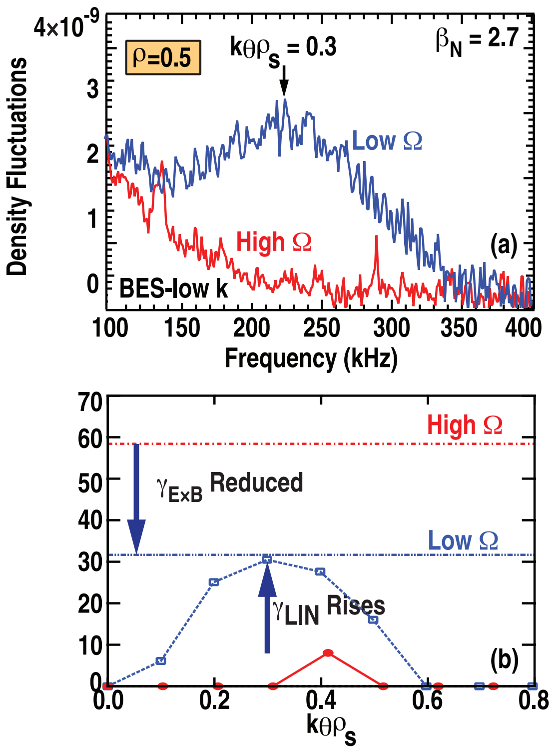

Figure 16. (a) Increase in low k turbulence at low rotation, measured by beam emission spectroscopy (b) GYRO predicted linear growth and $E \times B$ shearing rates for these cases.

this physics, transport studies have focused on how turbulence, transport and confinement change approaching burning plasma conditions: low applied torque and higher electron heating.

Experiments that systematically varied torque demonstrated for the first time the radial and wavenumber dependencies of the $E \times B$ shear paradigm of turbulence suppression [37]. These reveal a sharp rise in low k turbulence $(0.1 < k_\perp \rho_s < 0.5)$, observed in density fluctuations from BES (figure 16(a)) near $\rho = 0.5$, correlated with a decrease in energy confinement at lower torque and toroidal rotation, while particle confinement exhibits a more modest change. This behaviour is matched by GYRO predictions of increased linear growth rates, as well as reductions in $E \times B$ shear rates (figure 16(b)). Interestingly, low k turbulence at radially outboard locations $(0.6 < \rho < 0.75)$ undergoes little change in turbulence amplitude with increasing $E \times B$ shear, despite the varying $E \times B$ shearing rates. Instead the turbulence exhibits shorter eddy lifetimes (and thus increased decorrelation rates), as well as a reduction in the poloidal wavenumber, consistent with theoretical models of $E \times B$ shear dynamics. These changes indicate that it is important to understand transport optimization in low rotation conditions, rather than rely on high levels of injected torque and rotation to suppress low k turbulence which might not apply in future reactors. The studies also highlight the role of rotation shear, suggesting techniques to raise this, such as through generating neoclassical toroidal viscosity with 3D field as used in QH-mode may help optimize performance.

Turning to electron heating, the sensitivity of density gradient driven trapped electron mode (TEM) turbulence to electron temperature and T_e/T_i [38] has been characterized and exploited to locally control the density profile with strong electron heating [39, 40] via ECH (figure 17(a)). Low rotation, high density QH-mode plasmas [41–43] provide a quiescent background to observe behaviour without sawteeth, ELMs or core MHD activity. When neutral beam heating is augmented with 3.4 MW ECH, stronger TEM scale density fluctuations are observed with DBS [44] measurements (figure 17(b)) in the inner core. A band of coherent fluctuations is observed, corresponding to adjacent toroidal mode numbers. Linear growth rate spectra from GYRO mirror the observed change in density fluctuation spectra with ECH. Nonlinear GYRO simulations of density gradient driven TEM turbulence during ECH reproduce the broadband frequency spectrum (figure 17(c), taken at a later time when density profiles have been flattened and coherent fluctuations are smaller), using a new synthetic diagnostic based on [45]. The same simulations also match particle and thermal fluxes in tightly constrained comparisons, with only 10% uncertainty in the density gradient, measured by the profile reflectometer. The TEM turbulence drives particle and momentum transport, as well as energy transport, leading to decreased density peaking and core rotation during electron heating. This suggests a possible self-limiting mechanism in burning plasmas, where increasing α power will drive more TEMs, thereby reducing density peaking.

These basic trends have also been observed in plasmas with dominant electron heating at lower β, where a transition from ion temperature gradient (ITG) to TEM behaviour is observed when NBI heating is replaced with ECH [46]. This leads to an increase in particle diffusion, as predicted by TGLF. Part of the increase in diffusion is countered by an increase in particle pinch, at those locations where an increase in intermediate scale density fluctuations are observed. DIII-D studies help explain ASDEX Upgrade results [47], which found an increase in density peaking with decreasing collisionality and rotation. Observations varied collisionality and rotation separately to find that increased $E \times B$ shearing rates, rather than collisionality or inward roto-diffusion (rotation gradient induced particle diffusion),

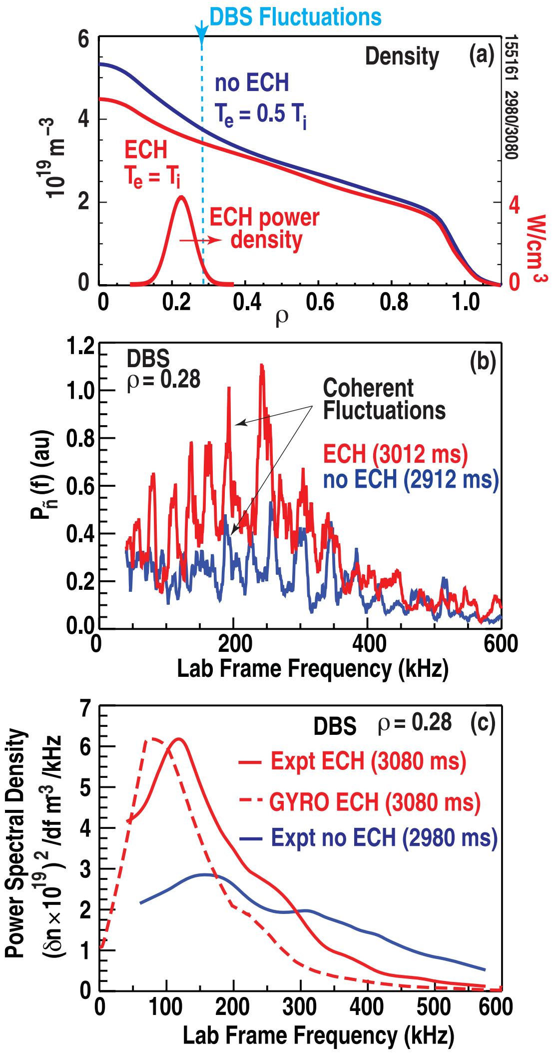

Figure 17. (a) Local flattening of density profile with electron heating in QH mode, leads to (b) increase in TEM density fluctuation level accompanying increased particle transport, also revealing new coherent TEM fluctuations. (c) nonlinear GYRO simulations of TEM turbulence, with synthetic DBS, reproduce the density fluctuation spectrum with ECH (binned in frequency).

suppress turbulence to alter profiles. Work has also continued to explore basic turbulent physics in dominantly electron-heated regimes, confirming the gyrokinetic and gyrofluid models (GYRO and TGLF) of stiffness in electron transport as TEMs become excited [48, 49]. However, ion heat flux remains under-predicted. These studies represent powerful tests of turbulence models, providing validation at three levels—profiles, transport and turbulence amplitudes and spatiotemporal properties—critical to projecting techniques to reach required performance in burning plasmas.

4.2. Fast ion behaviour

Fusion energy requires good confinement of energetic fast ions for efficient heating and current drive. However, fast ions can drive Alfvén eigenmodes (AEs), which in turn redistribute the fast ions, as observed in some steady state plasmas [50]. Experiments on DIII-D have identified a critical gradient behaviour behind this effect. It is found that as the fast ion pressure gradient rises above a threshold, redistribution effects rise rapidly (figure to appear in forthcoming paper [51]) leading to a limit in fast ion density [52]. This behaviour is hypothesized to be due to overlap of many small amplitude AE resonances. This potentially transforms predictive capability, greatly easing projection to future facilities. The work is complemented by comparisons to the first comprehensive fully nonlinear simulations of AE and fast ion evolution [53, 54], which match mode structure and saturation levels well, confirming the physics on which critical gradient models are founded.

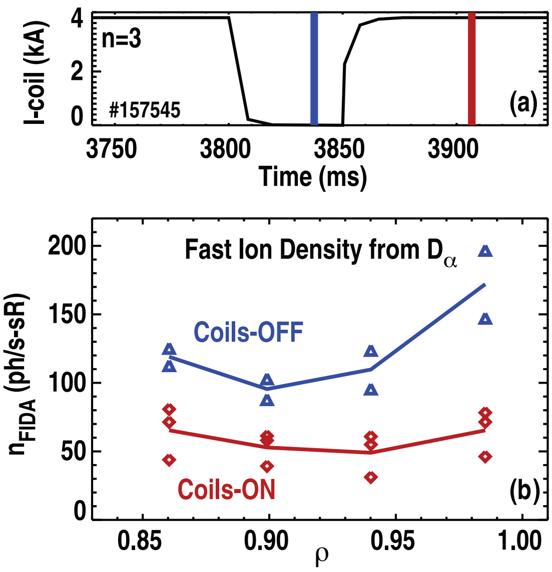

Figure 18. Fall in fast ion density (b) as RMP (a) turns back on, after brief period switched off (spatial profiles at times indicated on top trace).

Fast ion redistribution can also lead to localized heating of the tokamak walls, particularly when 3D fields are present. For example, figure 18 shows how RMP fields used for ELM suppression can eject a significant fraction of confined fast ions in the plasma edge region [55, 56]. Here brief notches in RMP field lead to rises in fast ion density while divertor heat loads fall substantially. Results are well represented by the SPIRAL full orbit code, which models the interaction of a realistic beam ion distribution with the 3D field, including ideal MHD response from M3D-C1. SPIRAL predictions show the majority of $n = 3$ induced EP losses originate from $\rho > 0.7$ and are deposited mostly to the divertor. Fast ion losses are also observed with internal modes such as neoclassical tearing modes (NTMs) and AEs. Further, losses from multiple modes can combine nonlinearly to lead to mechanisms for greatly enhanced ion loss. This highlights the importance of optimizing 3D field geometry to minimize fast ion losses, as also discussed in the TBM error field correction mentioned in section 5.1.

5. Realizing stable integrated burning plasma scenarios

The optimization of operating scenarios for burning plasma conditions raises key challenges for stability and scenario development. Low torque operation makes the plasma more

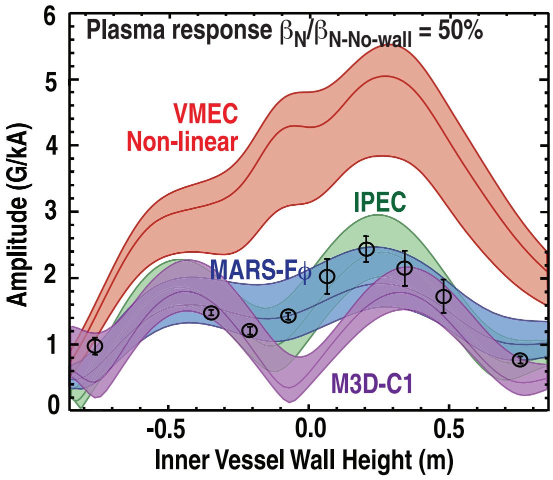

Figure 19. Amplitude of magnetic response at the high-field side wall to an $n = 1$ perturbation applied at the low-field side, comparing measurements (circles) versus predictions by several MHD models. The width of the bands indicates uncertainty associated with the equilibrium reconstruction used as input to the models.

susceptible to MHD driven by 3D 'error' fields or inherent instability; this behaviour must be understood and better controlled. Techniques for establishing ELM control and radiative divertor conditions must be integrated. Regimes need to be re-optimized for transport and pedestal behaviour in burning plasma relevant conditions.

5.1. Interaction of 3D fields with fusion plasmas

A foundational issue is the response of the plasma to 3D fields—effective models are critical to understanding how to optimize their use for control and avoid deleterious 'error field' effects. To explore this a major upgrade to the DIII-D magnetics diagnostic was implemented [57] including improved high-field side arrays that allow spatially resolved measurements of the plasma's response to external 3D fields. Measurements of the response to an $n = 1$ helical field applied with low-field side coils ('I-coils') show that linear, ideal MHD models (e.g. MARS-F and IPEC) describe the structure of the response well [58] (figure 19). Two-fluid M3D-C1 simulations also agree well but reveal sensitivities to assumptions on edge conductivity and single/two fluid MHD, while a non-perturbative MHD simulation (VMEC) tends to over-predict the response; analysis is now focusing on an apparent numerical artefact in the VMEC code which leads to an $m = 1$ $n = 2$ current filament in the core.

Thus ideal MHD plays a major role in 3D field response, and further experiments show that this is primarily governed by a single 'least stable' ideal mode for $n = 1$ fields. This is confirmed by experiments measuring neoclassical toroidal viscosity (NTV) braking of plasma rotation [59–61]. figure 20(a) shows measured toroidal angular momentum (from CER rotation Thomson density profiles) in plasmas where C- or I-coils are applied separately, and then when combined together in such a way as to cancel out ('null') coupling to the $q = 2$ surface through ideal MHD. It is found that while fields from internal and external coil arrays separately lead to braking, combining them to null out coupling

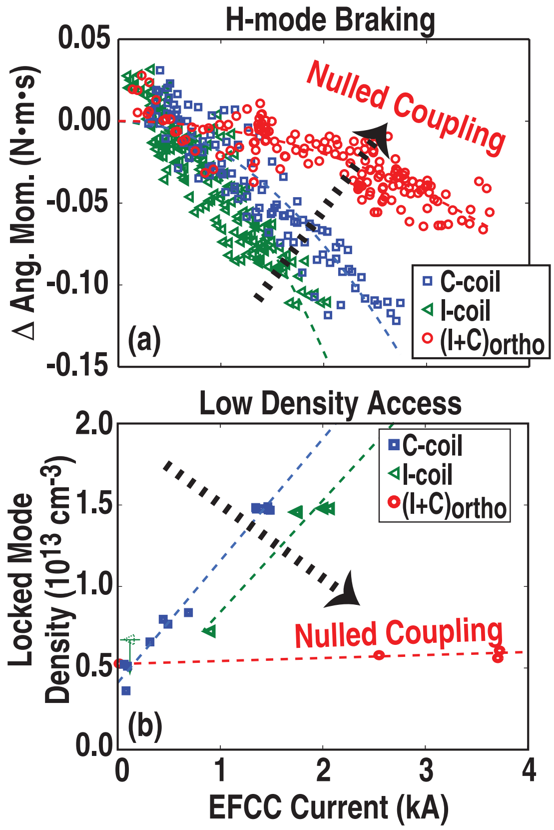

Figure 20. Fields with nulled coupling to the least stable ideal mode (red circles) have a weak effect on plasma rotation (a) (measured in terms of angular momentum of the plasmas) and on the locked mode density threshold (b) (different experiments to (a)), enabling operational space to be recovered by nulling the coupling in both cases (black dashed arrow) compared to cases with I- or C-coils applied separately (blue squares, green triangles).

to the least stable ideal mode reduces most of the braking effect. This cancellation also carries over to locked mode threshold. figure 20(b) shows other plasmas in which density was ramped down or 3D was field ramped up until an $n = 1$ locked mode was induced. Again, it is found that while individual I or C coil fields substantially raise the minimum density that can be accessed without locked modes, the 'nulled coupling' field combining C and I coils leads to negligible rise in density threshold, even at very high-field amplitudes. The consistency between these two very different approaches, one based on localized flux surface field penetration and the other on global braking, is further evidence of a single mode response for $n = 1$ fields. This positive result indicates 3D error field effects may be readily compensated through correction that minimizes just one component of the field. The work has also established a non-disruptive means of optimizing error correction through plasma rotation in DIII-D.

Single-component error field compensation has been applied to the key challenge of the Test Blanket Module (TBM) in ITER. In high rotation variants of the ITER scenario, a TBM simulator in DIII-D is found to cause significant localized heat loads to TBM armour tiles from fast ion loss accompanied by modest confinement degradation and plasma braking (figure 21, blue traces). However, using a fixed structure empirically optimized $n = 1$ correction

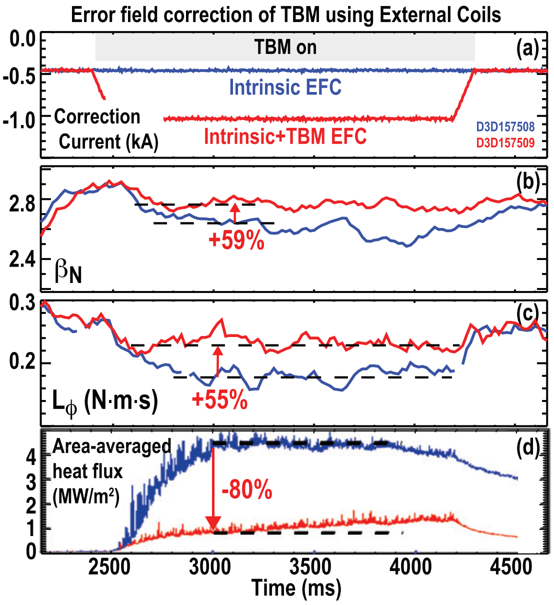

Figure 21. TBM energized from 2.4 to 4.3 s (a) (blue case) leading to degradation in β_N (b), angular momentum (c) and increased heat load (d), alleviated by correction currents (red case) to give recovery in β_N, plasma angular momentum (L_φ) and local heat flux near TBM.

field generated by ex-vessel control coils, the localized heat flux is reduced by 80% (red traces), while more than half the degradation in β_N and toroidal angular momentum is recovered. At low torque the TBM is found to have more serious effects, slowing the plasma, leading to rotation collapse and locked mode disruption in ITER baseline-like plasmas (figure 22). Here too, careful tailoring of $n = 1$ correction fields is found to avoid the worst effects, preventing rotation locking to permit operation even at virtually zero torque and TBM field strengths equivalent to the linear sum of three ITER TBM modules (a worst case scenario), opening the operational window for ITER (figure 22). (It should be noted that additional $n = 2$ correction fields provided little further benefit). These results highlight the importance of good error field correction, with partial correction narrowing the window of stable low torque operation (yellow, figure 23). Further, with ITER plasmas likely to be lower in collisionality than those used here, there could be additional non-resonant braking effects in ITER if residual error fields are permitted. These results are nevertheless highly encouraging that the proposed design and quantity of ITER TBM material is compatible with its performance goals, provided good error field correction is deployed.

5.2. ECCD control of tearing modes

The other critical stability issue for ITER is tearing modes. Previous tools for real time tearing control with localized electron cyclotron current drive (ECCD), have been upgraded with: (1) faster more accurate mirrors, (2) real-time Thomson electron temperature and density acquisition and fitting as input to the real-time TORBEAM code for ECCD aiming locations along with (3) the real-time MSE-EFIT for q-surface locations. This enabled the technique to be applied in evolving high β_N

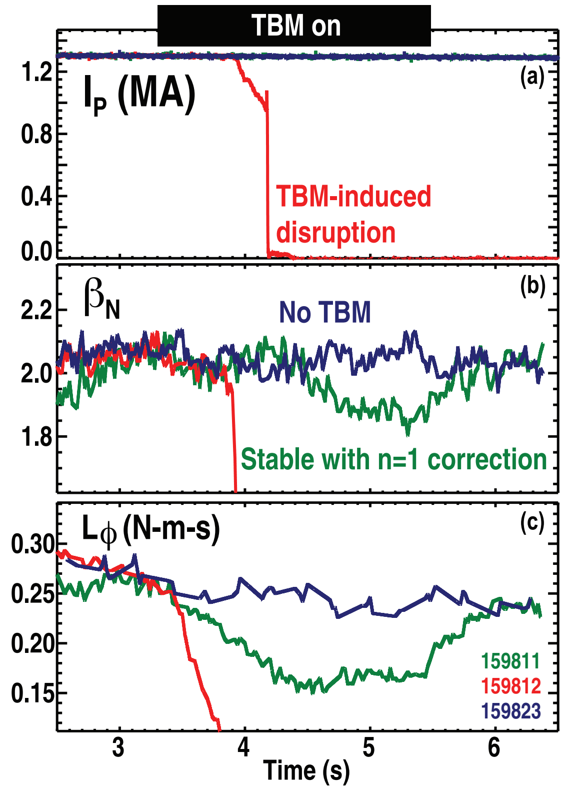

Figure 22. Correction of the TBM error field avoids disruption (plasmas current) (a), in the low torque ITER baseline scenario to maintain β_N (b) and angular momentum (c).

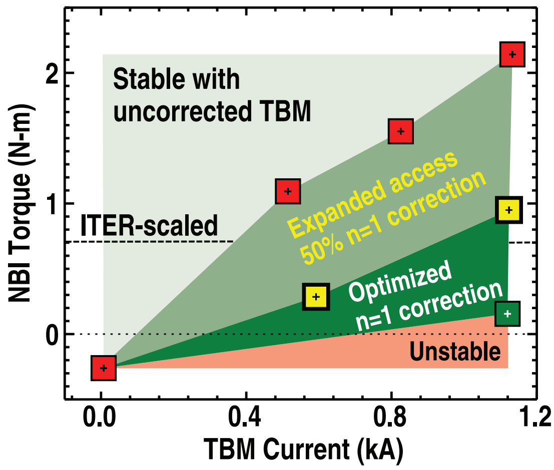

Figure 23. Access to low-torque operation as function of TBM field amplitude with optimized $n = 1$ correction (green), partial (50%) correction (yellow), and uncorrected (red squares). ITER scaled torque is 0.8 N m.

scenarios such as the 'high l_i' regime, the high $q_{min} > 2$ advanced tokamak, as well as the ITER baseline scenario. In the high l_i regime (figure 24) tracking is maintained as the discharge evolves, with mode control only lost when the ECH power (upper panel) and current drive fall too low, evident in the growth of a 2/1 mode (lower panel). In the $q_{min} > 2$ advanced tokamak scenario (not shown here) tracking at $q = 3$ kept a 3/1 tearing mode from becoming unstable. Finally in the ITER baseline scenario, the ECCD prevented development of a 3/2 tearing mode until a 2/1 mode

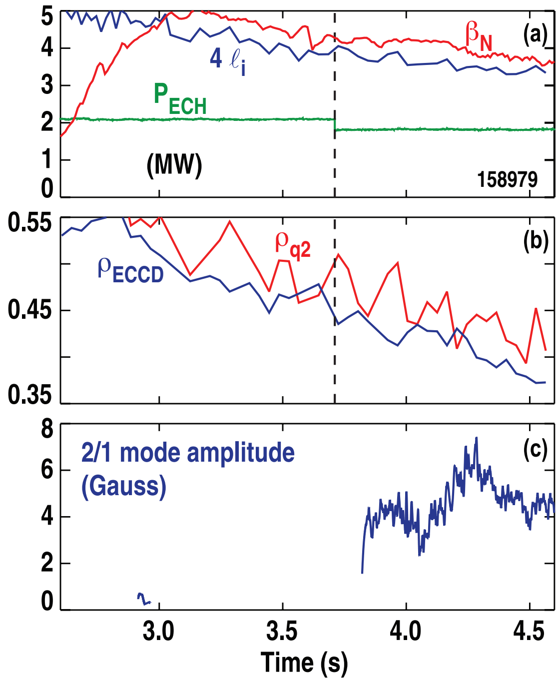

Figure 24. Application of real time NTM mode tracking (b) with ECCD at high β_N in the high l_i scenario (a) avoids modes (c) until ECH power (a) is reduced.

appeared, was detected and the mirrors redirected the ECCD to $q = 2$ to enable the 2/1 locked mode to be stabilized, avoiding a disruption and recovering H-mode. Thus the techniques for real time steerable ECCD have been developed and demonstrated to establish robust and flexible mode control to maintain stability. It should be noted that in some of these regimes, beneficial effects on stability and mode avoidance are also found without precise alignment of broader ECCD to the resonant surface, indicating further work is needed to understand the mechanisms governing tearing stability.

5.3. Approach to the ITER baseline

To maintain high Q operation in ITER, it is highly desirable to avoid the use of ECCD tearing mode control techniques, particularly those that require continuous application of ECCD. However, maintaining stability becomes more challenging as low torque conditions are approached for the ITER baseline, where the rotation profile can spontaneously become hollow, with modes tending to co-align, leading to rotation collapse and usually disruption. Maintaining stability requires good error field correction and strategies to avoid the triggering and the onset of tearing modes. Encouragingly, work has found that stability to low n tearing modes is improved when a low torque start up is applied. (The origins of this are still being investigated). Such modes tend to be destabilized more often in high torque startups, and while these can be relatively benign while the torque remains high, they tend to lock when torque is ramped down. However, at low torque, infrequent ELMs and an associated impurity build up can still lead to increased 3/2 or 2/1 instability and rotation collapse. Here, ELM pacing with I-coil modulation proved effective in triggering more rapid ELMs that avoided

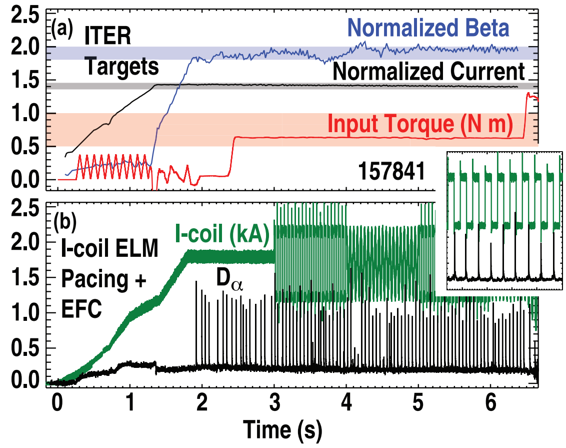

Figure 25. ITER baseline demonstration at low torque without the need for ECCD NTM control (normalized current is I/aB), with pedestal regulation through RMP ELM pacing. ITER target parameters are shown by the corresponding colour shaded regions in (a). (b) Shows I-coil current (green) and ELMs (black) with the insert to show pacing to I-coil pulses.

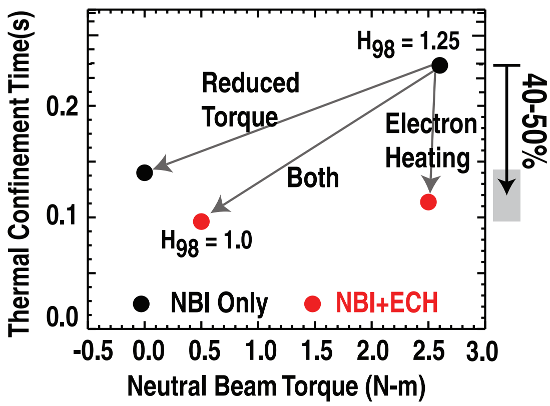

Figure 26. Reductions in thermal confinement as more ITER-relevant conditions are approached in terms of electron heating and injected torque.

impurity accumulation and the tearing mode. This enabled demonstration of a $Q_{eq} = 10$ ITER baseline at low torque without the need for ECCD mode control (figure 25) [62].

In developing these plasmas, it should be noted that increasing fidelity to ITER conditions was found to significantly degrade confinement over usual co-NBI ion heated discharges on which the scalings to project to ITER were based (figure 26). Reducing torque and increasing electron heating each led to significant confinement degradations, requiring large rises in auxiliary heating power to recover lost stored energy (and thus fusion performance in ITER). Nevertheless, the effect of these two degradations is not additive, and performance remains marginally acceptable for the ITER baseline in the reduced torque electron-heated regime, meeting the $H_{98pby,2} = 1$ requirement that enables 500 MW of fusion power with available heating systems. Here, $H_{98pby,2}$ falls more modestly than confinement time itself because although significantly more heating power (a factor 2) is needed to maintain β, a confinement degradation with heating power is built into the confinement scaling law for $H_{98pby,2}$. Nevertheless, this doubling of required heating power

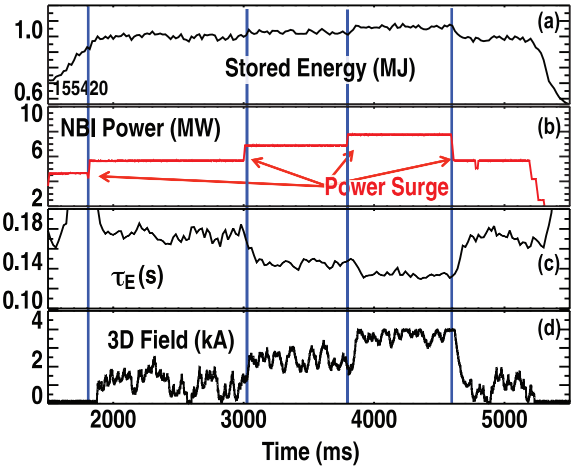

Figure 27. Real time 3D pedestal regulation will provide effective burn control. Here 3D fields (d) respond to changes in stored energy (a) to limit its rise as neutral beam power is increased (b), by reducing confinement (c). The 3D field spectrum and amplitude used here are similar to that used for RMP ELM control.

when switching from high torque ion heating to low torque electron heating, is a substantial concern for ITER.

In a final development, a technique for burn control has been developed [63] using $n = 3$ 3D fields from the I-coils to regulate pedestal height and confinement to deliver nearly constant stored energy despite significant power excursions (figure 27). This provides a useful basis for fast regulation of fusion power in ITER.

Turning to the future, the various degradations observed as one integrates the required conditions, and additional techniques such as ELM and radiative divertor control, motivate further effort to recover performance. Thus studies will target how to favourably combine elements of ELM amelioration with effects that improve transport and stability, such as through profile modification (as demonstrated with hybrid regimes) or neoclassical toroidal viscosity (to add $E \times B$ shear as appears favourable in QH-mode), to achieve $Q_{eq} = 10$ more robustly with better margin, and if possible with reduced current to lower disruption risks.

6. The path to steady-state fusion

To achieve steady-state fusion requires a predominantly self-driven plasma current and high β_N. Here, transport, stability and current profiles become mutually dependent—a self-consistent solution must be found and behaviour at high β_N understood. DIII-D has used its flexible heating and current drive systems to make advances on three promising paths.

6.1. 'High q_{min}' scenario with broad profiles

For a fusion power plant, scenarios with high β_N potential are key to optimizing bootstrap current and fusion performance. High-q_{min} scenarios exploit broad current and pressure profiles (using DIII-D's off axis neutral beams and ECCD) to raise the wall-stabilized ideal MHD β_N limit and bootstrap current. Operation with $q_{min} = 2$–2.5 and $q_{95} = 5$–7 has been investigated with relatively low density ((3.5–4.5) $\times 10^{19}\,\mathrm{m}^{-3}$) and 2.5–3.5 MW off-axis ECCD to maximize the noninductive

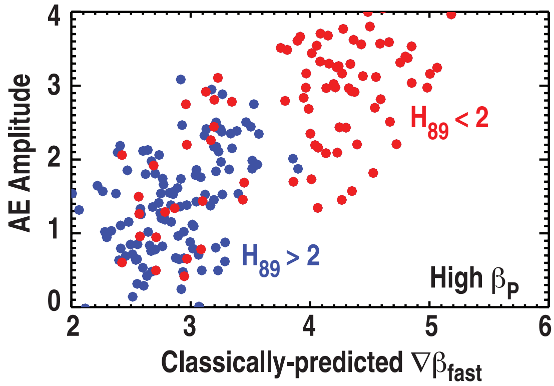

Figure 28. Increased fast ion gradient leads to increased Alfvén eigenmode amplitude and reduced confinement. Here Alfvén eigenmode activity is plotted against classically predicted fast ion gradient (as a measure of AE drive). A correlation with confinement is found (red points, $H_{89} < 2$ compared to blue points $H_{89} > 2$.

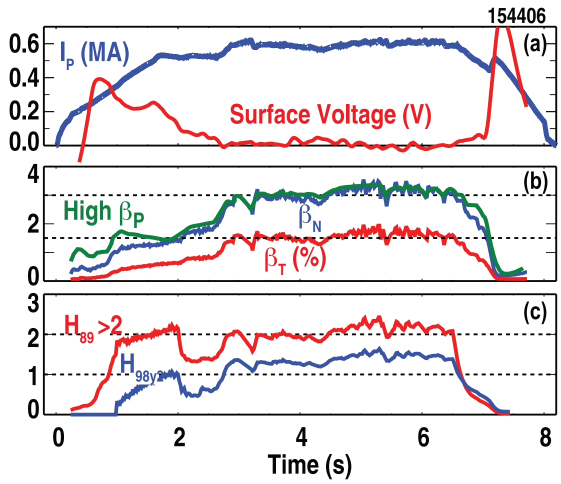

Figure 29. Fully noninductive high β_P regime demonstrates good confinement. Good confinement (c) leads to high β (b) and zero surface voltage (a), thus maintaining plasma current without solenoid ramping.

current fraction at reactor-relevant β_T. However, this regime is observed to have lower than expected global energy confinement ($H_{89P} = 1.6$–1.8), which is thought to be associated with AE- induced fast-ion transport [64].

This interpretation is confirmed by extending the scenario to high β_P, with $q_{min} = 3$–5, $q_{95} = 11$–12, and density $=$ (5–6.5) $\times\ 10^{19}\,\mathrm{m}^{-3}$. Here, the fast ions thermalize more quickly via electron drag, keeping the fast-ion β at or below a critical gradient for fast ion driven instabilities, as discussed in section 4.2. figure 28 demonstrates this, with increased fast ion gradient drive, as represented by the classically predicted fast ion gradient $\nabla\beta_{fast}$, correlating with increased Alfvénic activity and reduced global confinement. Optimizing to avoid this activity leads to excellent global ($H_{89P} = 2.3$) and thermal confinement ($H_{98pby,2} = 1.5$). Fast-ion confinement is nearly at the classical level while an internal thermal transport barrier exists. These plasmas are sustained with 80% bootstrap current for two current redistribution timescales (figure 29), providing a demonstration of fully noninductive stationary

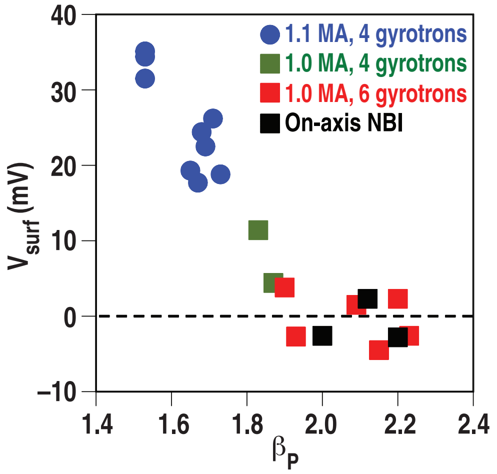

Figure 30. 1 MA fully noninductive steady state hybrid regime achieved with efficient on-axis current drive. Here, increases in β_P and ECCD lead to zero surface voltage.

conditions [65, 66], as well as a suitable target regime for long pulse assessments in the superconducting EAST facility [67, 68].

This work highlights an important consideration on the path to high performance steady states, where higher I_P and $\beta_T$are needed for a higher equivalent Q ($q_{95} = 5$–7). To meet this goal it will be important to avoid excessive peaking of fast ion distributions and performance degradation, which will be explored on DIII-D with planned increases in off-axis neutral beam power and ECH.

6.2. Hybrid scenarios

For a Fusion Nuclear Science or Component Test Facility (FNSF/CTF), a more centrally peaked current and higher performance 'hybrid' scenario has been developed using neutral beams and ECCD to sustain 1 MA current fully noninductively (figure 30) at $\beta_N = 4$ and 40% Greenwald density [69]. 50% externally driven current combines with 50% bootstrap to sustain the discharge in stationary conditions for more than a current redistribution time-scale. Confinement is excellent ($H_{98pby,2} = 1.7$), optimizing towards higher density, with peak β_N values limited to 4.3 by energetic particle and tearing modes. The current profile is anomalously broadened by a benign $m/n = 3/2$ tearing mode that maintains $q_{min} > 1$ even with a large amount of on-axis external current drive. This raises the possibility of sustainment using maximally efficient on-axis current drive—an attractive option for an FNSF or ITER that will not need extremely high bootstrap current fractions to meet stated goals. Encouragingly, RMP-ELM suppression has also been demonstrated in the ITER-shaped plasmas in this scenario [8].

6.3. 'High l_i' scenarios with peaked current profile

An alternative path to steady states lies in plasmas with a still more peaked current profile—the 'high l_i' scenario [71, 72]. This can raise the ideal MHD limit to $\beta_N > 5$, while offering excellent confinement. Here, the current profile was

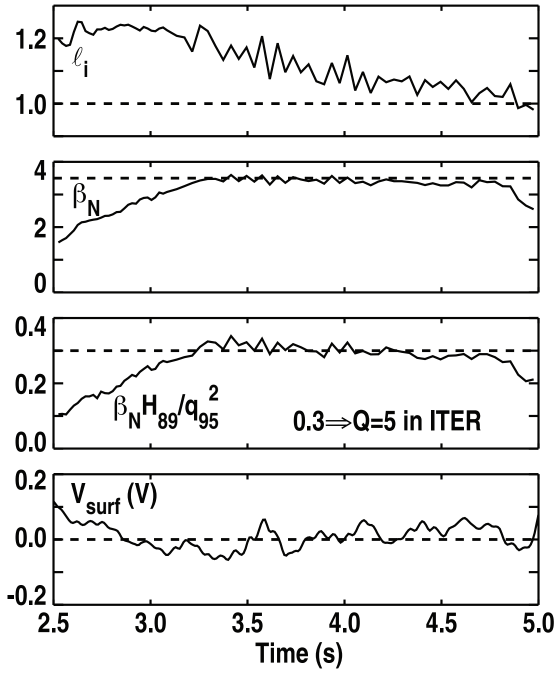

Figure 31. Fully noninductive high l_i scenario meets ITER performance goals (dashed lines) for its steady state mission.

optimized through pre-forming at low β_N and then slowing its evolution to a less favourable profile through electron heating and ECCD, in order avoid the β collapse following the first ELM that terminated previous attempts. In an ITER shape this led to transient performance (measured in terms of $\beta_N H_{89}/q_{95}^2$) consistent with a projected $Q = 5$ discharge in ITER (figure 31), making high l_i an attractive candidate for ITER steady state using its day-one heating systems. In a double-null shape, β_N close to 5 was achieved (figure 24) with $H_{98y,2} = 1.8$ and 80% bootstrap current, leading to some current overdrive. Full stationarity is predicted with planned increases in ECH current drive power.

7. Developing a boundary solution for fusion energy

A boundary solution for future reactors represents one of the remaining grand challenges for fusion energy. This must go beyond present radiative techniques to establish an essentially detached, erosion free divertor. It requires optimization in divertor geometry and the plasma–materials interface (PMI). Thus, a new initiative has been launched to develop the basis for next-step fusion development, to be tested in DIII-D.

7.1. Detachment physics

Experiments have identified key trends on divertor detachment and shortfalls in its present understanding. Significant progress has been made in model validation, reproducing divertor parallel transport along field lines in well-attached plasmas. New 2D mapped divertor Thomson scattering measurements show a sharp transition to detachment with increasing separatrix density (figures 32(a) and (b)) [73, 74], which is presently not easily reproduced in simulation. Encouragingly, confinement is not found to fall abruptly

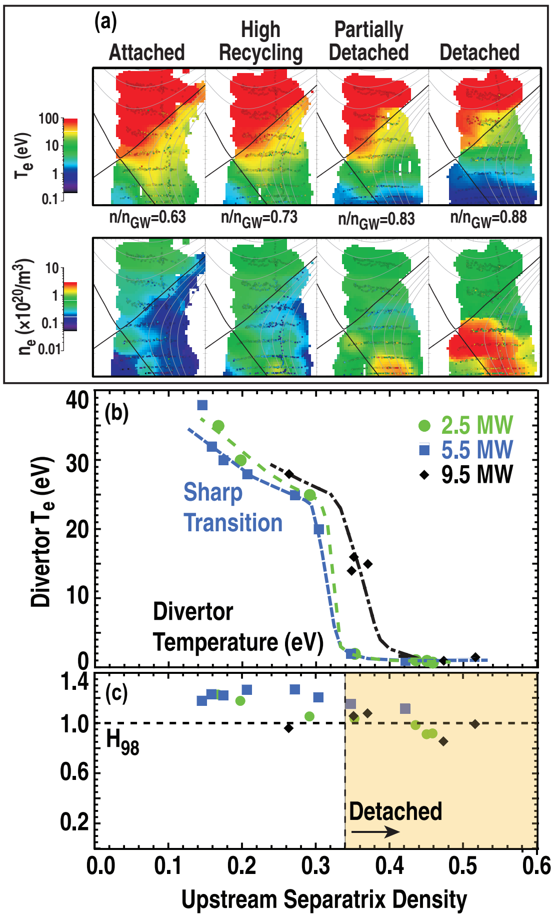

Figure 32. High resolution sub-eV Thomson scattering measurements (a) characterize a sharp transition to detachment (b) as upstream separatrix density is raised, although H_{98} does not exhibit a correspondingly abrupt fall as the plasma detaches (c).

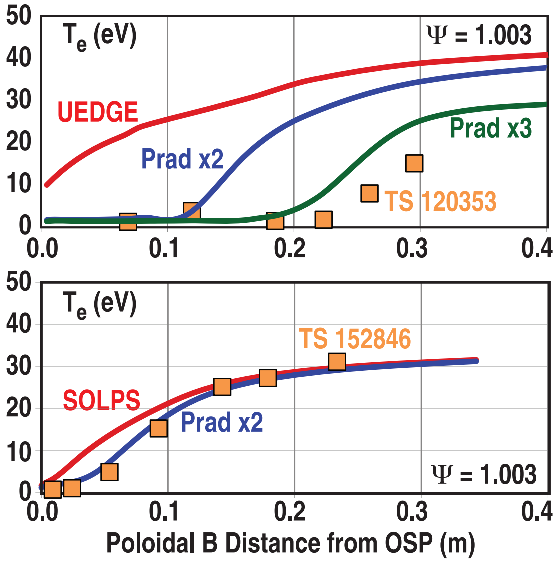

Figure 33. Detachment shortfall between experiment (squares) and simulation codes (curves) with various radiation assumptions relative to model for L-mode plasmas: (a) UEDGE code, (b) SOLPS code. Temperature is plotted against distance from the outer strike, as measured in a poloidal plane projection.

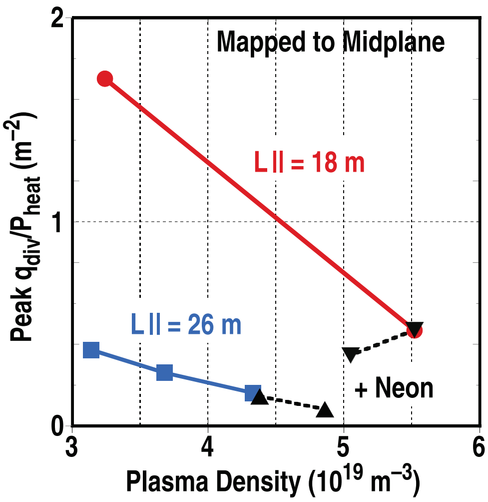

Figure 34. Connection length effect on peak divertor heat flux (normalized to heating power) on approach to detachment as density is varied. Adding neon further reduced peak heat flux.

with the onset of detachment, though there is a modest degradation over the larger range in density (figure 32(c)). Comparison of detachment data with simulation reveals a radiation shortfall in L-mode plasmas (figure 33), with the UEDGE and SOLPS models only matching the experimental radiated power data once carbon levels are raised above experimental levels, suggesting improved treatment of cold, molecular and atomic species is needed. H-mode comparisons yield a similar shortfall, though it is important to note further discrepancies at intermediate densities in predicted strike point plasma temperatures. Interestingly, helium plasmas detach at a higher temperature (3 eV) than deuterium (∼1 eV), suggesting that molecular radiation may play an important role in D_2 plasmas.

Plasma geometry is a key element in divertor optimization, with increased parallel and poloidal connection length found to detach plasmas more readily at lower core densities (figure 34) [75]. As divertor leg length is increased, increasing radiative power and cross-field transport play an important role in reducing heat flux to the divertor. Similarly, a snowflake divertor leads to a decrease in peak scrape-off layer heat flux compared to standard divertor configurations [76]. Upstream scrape-off layer profiles exhibited a critical gradient behaviour, consistent with ideal ballooning limits and measured divertor target heat flux widths from low density up to divertor detachment. These elements are helping improve models for developing advanced divertor concepts.

7.2. Integrated scenarios

Techniques to enhance edge and divertor dissipation have been integrated into steady state and inductive plasma operating scenarios yielding good performance and insights into optimization. It is found that impurity accumulation from a neon radiative divertor could be controlled by D_2 puffing to yield 80% radiation in ITER scenarios [75]. In steady-state scenario DND plasmas, neon injection into the private flux region away from the ion $B \times \nabla B$ direction reduces core impurity rises, to maintain $H_{98pby,2} = 1.3$ performance while halving divertor heat flux (figure 35). Steady state has also been

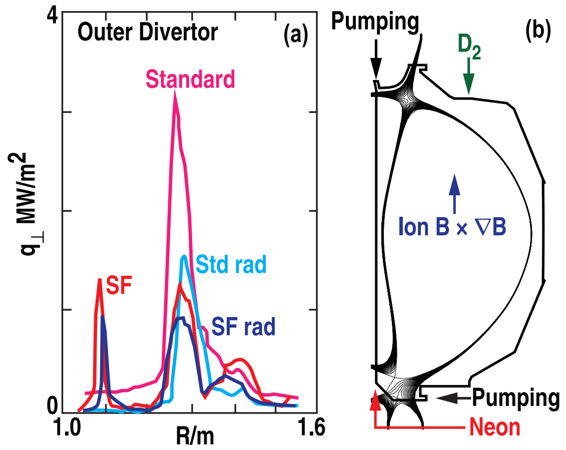

Figure 35. Radiative standard and snowflake divertors with steady-state scenario plasmas: peak heat flux (a) and configuration shape (b).

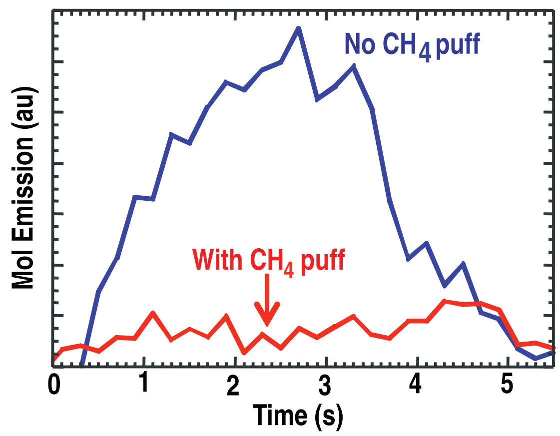

Figure 36. Low-Z coating (CH_4) prevents high-Z erosion as observed in molybdenum line emission.

combined with the radiative snowflake divertor to yield modest further reductions in heat flux compared to standard radiative divertor, although the snowflake also reduces impurity control.

7.3. Plasma–materials interactions

DIII-D also provides an important qualifying stage for developing plasma facing component (PFC) solutions using the Divertor Material Evaluation System (DIMES) to expose and study plasma–material interactions in tokamak plasmas [77]. Experiments have confirmed net erosion of tungsten divertor surfaces to be weak, with gross erosion largely compensated by re-deposition. This work validated models that indicate low net erosion in the ITER divertor. For areas of particular concern outside the divertor, a new technique is demonstrated with renewable low-Z coatings that are found effective in reducing erosion. CH_4 puffing near the sample leads to a carbon layer and factor of >10 reduction in molybdenum erosion (figure 36). This paves the way for other low-Z elements (B, Si, Li) as potential protective layers against transients such as large ELMs or disruptions. Studies are now turning to validation of advanced materials for the reactor environment through testing of samples exposed in linear facilities such as PISCES.

8. Conclusions and future plans

8.1. Summary

DIII-D has made important progress in developing solutions for ITER and a foundation of understanding to project behaviour, reach required performance and establish design requirements for future fusion reactors.

For ITER, DIII-D has made significant progress in developing and projecting the required techniques to enable its $Q = 10$ mission. On the critical challenge of disruptions, shattered pellet techniques have proven effective at directly quenching an emergent runaway beam, while new measurements identify pitch angle scattering as the origins of greatly increased runaway electron dissipation rates. Studies of the thermal quench process show low levels of toroidal radiation asymmetry when mitigation techniques are applied, even with a single gas valve, and confirm NIMROD interpretations of behaviour governed by an underlying 1/1 mode. Stability control has been developed to enable the ITER baseline at low torque, without the need for continuous ECCD mode stabilization, and this work is underpinned by improved understanding of 3D field interactions with a single dominant mode model explaining behaviour and allowing optimization of error field control strategies. This has been extended to cases with error field produced by a test blanket module (TBM) simulator, showing avoidance of otherwise disruptive modes that arise from TBM induced rotation collapses. Turbulence properties are also found to alter as less torque and more electron heating are applied, leading to increased low k activity, particle and thermal transport. While this validates key simulation projections, a note of caution must be added as increasing fidelity to ITER conditions is found to decrease performance, motivating further work to develop improved scenarios that recover performance.

Research has also advanced understanding of the H-mode pedestal to project how to achieve the required performance and control in ITER. In particular, the physical mechanism for RMP ELM suppression has been identified as resonant field penetration, with the technique shown robust to reduced coil set and Helium operation. The alternative technique of QH mode with a benign EHO has been shown compatible with high Greenwald density fraction and the EHO is found to give good levels of impurity flushing. Pedestal performance has been extended to a new 'super H mode' regime with doubled pedestal height through navigating a valley of improved stability predicted by the EPED model, while a key concept behind the EPED model, the role of the KBM, is confirmed by new turbulence measurements. Rotation is found to be generated locally in the pedestal through a kinetic loss mechanism distorting the plasma Maxwellian. L–H transition studies identify that while turbulence can induce H-mode through energy transfer to flows, the development of pressure driven ion diamagnetic flows play the key role in locking in the transition.

DIII-D continues to address critical issues underpinning projection to fusion energy. Energetic particles were found to exhibit a critical gradient behaviour associated with overlapping of multiple resonances. This is found to play a crucial role in limiting confinement of 'high $q_{\min}$' steady-state scenario discharges, where strategies to reduce fast ion peaking have proven effective in reaching high performance, including a fully noninductive high β_P discharge as a target for EAST. Results justify planned increases in off axis heating and current drive for more power plant relevant performance in DIII-D. An alternative 'high l_i' path with peaked profiles has been demonstrated by pre-forming profiles and deploying tearing mode control strategies. In single-null form, this shows promise for ITER's steady state mission with 'day 1' heating systems, while it may enable an alternative reactor solution in double null form, with $\beta_N > 5$ achieved. For a driven device such as a nuclear science facility, a hybrid scenario offers excellent potential, demonstrating 1 MA of fully noninductive current, excellent confinement, and a core instability that regulates the current profile to a stable solution.

Finally DIII-D is developing the physics basis for an improved boundary solution, required for fusion energy. New 2D mapped divertor Thomson scattering measurements identify a radiation shortfall in detachment models, while plasma geometry studies identify the key role of connection length in achieving high performance detached operation. PMI studies confirm low net erosion of tungsten divertor surfaces, while techniques to deposit renewable low-Z coatings are found highly effective in reducing erosion. Radiative and snowflake divertor operation has been successfully integrated with high performance steady state core scenarios demonstrating good performance while reducing divertor heat flux by a factor of two. However, these techniques will need to go considerably further for a future high power steady state fusion reactor, as discussed below.

These developments provide key solutions for ITER and a foundation of understanding in order to project behaviour and develop the means to safely achieve the required performance in future fusion reactors.

8.2. Future plans

Turning to the future, studies in DIII-D will focus on three synergistic initiatives, where anticipation of behaviour and development of new solutions is vital to the development of fusion energy at the reactor scale.

(i) *Prepare for burning plasmas* to anticipate the changes in thermal, particle, momentum and fast ion transport that will happen with low torque electron heating dominant conditions by deploying toroidally steerable beams and ECH in order to understand the behaviour and optimization of fusing plasmas.

(ii) *Determine the path to steady state* to develop a high β, self-consistent, fully noninductive, predominantly self-driven solution for fusion energy and an FNSF, with increased off-axis heating and current drive by increasing both the neutral beam total and off-axis power, ECCD and developing helicon ultra-fast wave current drive [78, 79], which has key potential for demonstrating high wall-plug to current drive efficiency compatible with future reactor requirements.

(iii) *Develop a boundary–PMI solution* to achieve an erosion free detached divertor solution compatible with a high performance self-driven core and PFC materials, by implementing an advanced divertor, reactor relevant hot walls and an advanced 3D field coil set.

These improvements will enable DIII-D to provide vital input to the ITER mission, in developing both the techniques to meet its performance goals and the models to project and interpret behaviour. However, they are even more critical for a future steady state reactor, such as DEMO or FNSF, which would be substantially advanced by further developments in core and boundary solutions that simultaneously achieve excellent fusion power output and acceptable power/particle exhaust.

Acknowledgments

This material is based upon work supported by the US Department of Energy, Office of Science, Office of Fusion Energy Sciences, using the DIII-D National Fusion Facility, a DOE Office of Science user facility, under Awards DE-FC02-04ER54698, DE-FG02-89ER54297, and DE-AC02-09CH11466. DIII-D data shown in this paper can be obtained in digital format by following the links at https://fusion.gat.com/global/D3D_DMP.

References

[1] Nazikian R. *et al* 2014 *Phys. Rev. Lett.* **114** 105002
[2] Paz-Soldan C. *et al* 2014 *Phys. Rev. Lett.* **114** 105001
[3] Snyder P.B. *et al* 2012 *Phys. Plasmas* **19** 056115
[4] Evans T.E. *et al* 2014 Comparative studies of static edge magnetic islands in DIII-D and LHD *25th IAEA Int. Conf. on Fusion Energy (St Petersburg, Russia 2014)* EX/1-3
[5] Ferraro N.M. *et al* 2013 *Nucl. Fusion* **53** 073042
[6] Ferraro N.M. 2012 *Plasma Phys.* **19** 056105
[7] Orlov D.M. *et al* 2014 Suppression of Type-I ELMs with incomplete I-coil set on DIII-D *25th IAEA Int. Conf. on Fusion Energy (St Petersburg, Russia 2014)* EX/P2-21
[8] Nazikian R. *et al* 2014 Advances in the understanding of ELM suppression by resonant magnetic perturbations (RMPs) in DIII-D and implications for ITER *25th IAEA Int. Conf. on Fusion Energy (St Petersburg, Russia 2014)* EX/1-1
[9] Snyder P.B., Groebner R.J., Hughes J.W., Osborne T.H., Beurskens M., Leonard A.W., Wilson H.R. and Xu X.Q. 2011 *Nucl. Fusion* **51** 103016
[10] Solomon W.M., Burrell K.H., Fenstermacher M.E., Garofalo A.M., Grierson B.A., Loarte A., McKee G.R., Nazikian R. and Snyder P.B. 2014 Advancing the physics basis of quiescent H-mode through exploration of ITER relevant parameters *25th IAEA Int. Conf. on Fusion Energy (St Petersburg, Russia 2014)* PPC/P2-37
[11] Solomon W.M. *et al* 2014 *Phys. Rev. Lett.* **113** 135001
[12] Liu F. *et al* 2014 Nonlinear MHD simulations of QH-mode plasmas in DIII-D *Proc. 41st EPS Conf. on Plasma Physics (Berlin, 2014)* O5.135 http://ocs.ciemat.es/EPS2014PAP/pdf/O5.135.pdf
[13] Grierson B.A., Burrell K.H., Garofalo A.M., Solomon W.M., Diallo A. and O'Mullane M. 2014 *Nucl. Fusion* **54** 114011
[14] Snyder P.B. *et al* 2014 Super H-mode: theoretical prediction and initial observations of a new high performance regime for tokamak operation *25th IAEA Int. Conf. on Fusion Energy (St Petersburg, Russia 2014)* TH/2-2
[15] Snyder P.B. *et al* 2015 Super H-mode: theoretical prediction and initial observations of a new high performance regime for tokamak operation *Nucl. Fusion* submitted

[16] Osborne T.H. *et al* 2015 Enhanced H-mode pedestals with lithium injection in DIII-D *Nucl. Fusion* in press
[17] Diallo A., Groebner R.J., Rhodes T.L., Battaglia D.J., Smith D.R., Osborne T.H. Canik J.M., Guttenfelder W. and Snyder P.B. 2015 *Phys. Plasmas* **22** 056111
[18] Yan Z., McKee G.R., Groebner R.J., Snyder P.B., Osborne T.H. and Burrell K.H. 2011 *Phys. Rev. Lett.* **107** 055004
[19] Diallo A. *et al* 2014 *Phys. Rev. Lett.* **112** 115001
[20] Battaglia D.J. *et al* 2014 Full-f neoclassical simulations toward a predictive model for H-mode pedestal ion energy, particle and momentum transport *25th IAEA Int. Conf. on Fusion Energy (St Petersburg, Russia 2014)* EX/P2-24
[21] Battaglia D.J. *et al* 2015 Full-f neoclassical simulations toward a predictive model for H-mode pedestal ion energy, particle and momentum transport *Nucl. Fusion* submitted
[22] Yan Z., McKee G.R., Fonck R., Gohil P., Groebner R.J. and Osborne T.H. 2014 *Phys. Rev. Lett.* **112** 125002
[23] Schmitz L. *et al* 2014 First direct evidence of turbulence-driven ion flow triggering the L- to H-mode transition *25th IAEA Int. Conf. on Fusion Energy (St Petersburg, Russia 2014)* EX/11.4
[24] Miki K., Diamond P.H., Gürcan Ö.D., Tynan G.R., Estrada T., Schmitz L. and Xu G.S. 2012 *Phys. Plasmas* **19** 092306
[25] Staebler G.M. and Groebner R.J. 2014 Limit cycle oscillations and L/H transitions from two dimensional mean field momentum transport equations *25th IAEA Int. Conf. on Fusion Energy (St Petersburg, Russia 2014)* TH/P5-12
[26] Staebler G.M. and Groebner R.J. 2015 Limit cycle oscillations and L/H transitions from two dimensional mean field momentum transport equations *Nucl. Fusion* in press
[27] Hollmann E.M. *et al* 2011 *Nucl. Fusion* **51** 103026
[28] Hollmann E.M. *et al* 2013 *Nucl. Fusion* **53** 083004
[29] Paz-Soldan C. *et al* 2014 *Phys. Plasmas* **21** 022514
[30] Hollmann E.M. *et al* 2015 *Phys. Plasmas* **22** 056108
[31] Commaux N. *et al* 2014 *Phys. Plasmas* **21** 102510
[32] Eidietis N.W. *et al* 2014 Measurement of radiated power asymmetry during disruption mitigation on the DIII-D tokamak *25th IAEA Int. Conf. on Fusion Energy (St Petersburg, Russia 2014)* EX/P2-22
[33] Izzo V.A. *et al* 2014 The role of MHD in 3D aspects of massive gas injection *25th IAEA Int. Conf. on Fusion Energy (St Petersburg, Russia 2014)* TH/4-1
[34] Izzo V.A. *et al* 2015 The role of MHD in 3D aspects of massive gas injection *Nucl. Fusion* in press
[35] Shiraki D., Commaux N., Eidietis N.W., Hollmann E.M., Izzo V.A. and Moyer R.A. 2014 *Bull. Am. Phys. Soc.* **59** 70
[36] Eidietis N.W. 2013 *Bull. Am. Phys. Soc.* **58** 107
[37] McKee G.R. *et al* 2014 Turbulence behavior and transport response approaching burning plasma relevant parameters *25th IAEA Int. Conf. on Fusion Energy (St Petersburg, Russia 2014)* EX/2-2
[38] Ernst D.R. *et al* 2004 *Phys. Plasmas* **11** 2637
[39] Ernst D.R. *et al* 2014 Controlling H-Mode particle transport with modulated electron heating in DIII-D and Alcator C-Mod via TEM turbulence *25th IAEA Int. Conf. on Fusion Energy (St Petersburg, Russia 2014)* EX/2-3
[40] Ernst D.R. 2012 *Bull. Am. Phys. Soc.* **57** 105
[41] Burrell K.H. *et al* 2001 *Phys. Plasmas* **8** 2153
[42] Doyle E.J. *et al* 2001 *Plasma Phys. Control. Fusion* **43** A95
[43] Greenfield C.M. *et al* 2001 *Phys. Rev. Lett.* **86** 4544
[44] Rhodes T.L., Peebles W.A., Nguyen X., Hillesheim J.C., Schmitz L., White A.E. and Wang G. 2010 *Rev. Sci. Instrum.* **81** 10D912
[45] Hillesheim J.C., Holland C., Schmitz L., Kubota S., Rhodes T.L. and Carter T.A. 2012 *Rev. Sci. Instrum.* **83** 10E331
[46] Mordjick S. *et al* 2015 Increase in edge rotation in ECJ heated DIII-D H-mode plasmas *Nucl. Fusion* submitted
[47] Angioni C. *et al* 2005 *Phys. Plasmas* **12** 040701
[48] Smith S.P., Petty C.C., White A.E., Holland C., Bravenec R., Austin M.E., Zeng L. and Meneghini O. 2014 Electron temperature critical gradient and transportstiffness *25th IAEA Int. Conf. on Fusion Energy (St Petersburg, Russia 2014)* EX/P2-29
[49] Smith S.P., Petty C.C., White A.E., Holland C., Bravenec R., Austin M.E., Zeng L. and Meneghini O. 2015 Electron temperature critical gradient and transport stiffness *Nucl. Fusion* submitted
[50] Heidbrink W.W., Ferron J.R., Holcomb C.T., Van Zeeland M.A. and the DIII-D Team 2014 Alfvén Eigenmodes can limit access to high fusion gain, steady-state tokamak operation *25th IAEA Int. Conf. on Fusion Energy (St Petersburg, Russia 2014)* EX/10-1
[51] Collins C., Heidbrink W.W., Van Zeeland M.A., Pace D.C., Stagner L., Zhu Y.B., Todo Y., White R.B. and Kramer G.J. 2015 Observation of critical gradient threshold for Alfvén eigenmode-induced fast-ion transport *Phys. Plasmas.* to be submitted
[52] Heidbrink W.W., Van Zeeland M.A., Austin M.E., Bass E.M., Ghantous K., Gorelenkov N.N., Grierson B.A., Spong D.A. and Tobias B.J. 2013 *Nucl. Fusion* **53** 093006
[53] Todo Y., Van Zeeland M.A., Bierwage A. and Heidbrink W.W. 2014 Multi-Phase Simulation of Alfvén Eigenmodes and fast ion distribution flattening in DIII-D experiment *25th IAEA Int. Conf. on Fusion Energy (St Petersburg, Russia 2014)* TH/7-1
[54] Todo Y., Van Zeeland M.A., Bierwage A. and Heidbrink W.W. 2015 Multi-Phase Simulation of Alfvén Eigenmodes and fast ion distribution flattening in DIII-D experiment *Nucl. Fusion* submitted
[55] Van Zeeland M.A. *et al* 2014 Fast ion transport during applied 3D magnetic perturbations on DIII-D *25th IAEA Int. Conf. on Fusion Energy (St Petersburg, Russia 2014)* EX/10-2
[56] Van Zeeland M.A. *et al* 2015 Fast ion transport during applied 3D magnetic perturbations on DIII-D *Nucl. Fusion.* in press
[57] King J.D. *et al* 2014 *Rev. Sci. Instrum.* **85** 083503
[58] King J.D. *et al* 2015 Experimental tests of linear and nonlinear 3D equilibrium models in DIII-D *Phys. Plasmas* submitted
[59] Paz-Soldan C. 2015 Limits of the single-mode model in the correction of high toroidal mode number error fields *Nucl. Fusion* submitted
[60] Paz-Soldan C. *et al* 2014 *Phys. Plasmas* **21** 072503
[61] Paz-Soldan C., Buttery R.J., Garofalo A.M., Hanson J.M., La Haye R.J., Lanctot M.J., Park J.-K., Solomon W.M. and Strait E.J. 2014 *Nucl. Fusion* **54** 073013
[62] Luce T.C. *et al* 2014 Expanding the Physics Basis of the Baseline Q = 10 Scenario Toward ITER Conditions *25th IAEA Int. Conf. on Fusion Energy (St Petersburg, Russia 2014)* PPC/2-34
[63] Hawryluk R.J. *et al* 2015 *Nucl. Fusion* **55** 053001
[64] Ferron J.R. *et al* 2013 *Phys. Plasmas* **20** 092504
[65] Garofalo A.M. *et al* 2014 Compatibility of internal transport barrier with steady state operation in the high bootstrap fraction regime on DIII-D *25th IAEA Int. Conf. on Fusion Energy (St Petersburg, Russia 2014)* PPC/P2-31
[66] Garofalo A.M. *et al* 2015 Compatibility of internal transport barrier with steady state operation in the high bootstrap fraction regime on DIII-D *Nucl. Fusion* submitted
[67] Gong X. *et al* 2014 Development of fully noninductive scenario at high bootstrap current fraction for steady state tokamak operation on DIII-D and EAST *25th IAEA Int. Conf. on Fusion Energy (St Petersburg, Russia 2014)* EX/P2-39
[68] Gong X. *et al* 2015 Development of fully noninductive scenario at high bootstrap current fraction for steady state tokamak operation on DIII-D and EAST *Nucl. Fusion* submitted
[69] Petty C.C. *et al* 2014 Achieving steady-state conditions in High-Beta Hybrid scenario in DIII-D *25th IAEA Int. Conf. on Fusion Energy (St Petersburg, Russia 2014)* PPC/P2-36
[70] Turco F. *et al* 2015 *Phys. Plasmas* **22** 056113

[71] Ferron J.R., Holcomb C.T., Luce T.C., Park J.M., Kolemen E., La Haye R.J., Solomon W.M. and Turco F. 2014 High internal inductance for steady-state operation in ITER and a reactor *25th IAEA Int. Conf. on Fusion Energy (St Petersburg, Russia 2014)* PPC/P2-35

[72] Ferron J.R., Holcomb C.T., Luce T.C., Park J.M., Kolemen E., La Haye R.J., Solomon W.M. and Turco F. 2015 High internal inductance for steady-state operation in ITER and a reactor *Nucl. Fusion* in press

[73] Kolemen E. *et al* 2014 Burning plasma relevant control development: advanced magnetic divertor configurations, divertor detachment and burn control *25th IAEA Int. Conf. on Fusion Energy (St Petersburg, Russia 2014)* PPC/1-1

[74] Kolemen E. *et al* 2015 Burning plasma relevant control development: advanced magnetic divertor configurations, divertor detachment and burn control *Nucl. Fusion* submitted

[75] Petrie T.W. *et al* 2015 Preliminary survey of application of the radiating divertor approach to innovative tokamak divertor concepts *Nucl. Fusion* submitted

[76] Soukhanovskii V.A. *et al* 2014 Developing physics basis for the radiative snowflake divertor at DIII-D *25th IAEA Int. Conf. on Fusion Energy (St Petersburg, Russia 2014)* EX/7-4

[77] Rudakov D.L. *et al* 2014 Reduction of net erosion of high-Z PFC materials in DIII-D divertor due to re-deposition and low-Z coating *25th IAEA Int. Conf. on Fusion Energy (St Petersburg, Russia 2014)* EX/P2-27

[78] Pinsker R.I. *et al* 2014 Off-axis current drive with high harmonic fast waves for DIII-D *25th IAEA Int. Conf. on Fusion Energy (St Petersburg, Russia 2014)* TH/P2-38

[79] Prater R., Moeller C.P., Pinsker R.I., Porkolab M., Meneghini O. and Vdovin V.L. 2014 *Nucl. Fusion* **54** 083024